



Evaluation of the VIIRS BRDF, Albedo and NBAR products suite and an assessment of continuity with the long term MODIS record



Yan Liu^{a,*}, Zhuosen Wang^{b,c}, Qingsong Sun^a, Angela M. Erb^a, Zhan Li^a, Crystal B. Schaaf^a, Xiaoyang Zhang^d, Miguel O. Román^b, Russell L. Scott^e, Quan Zhang^f, Kimberly A. Novick^f, M. Syndonia Bret-Harte^g, Shelley Petroy^h, Mike SanClements^h

^a School for the Environment, University of Massachusetts Boston, Boston, MA, USA

^b Terrestrial Information Systems Laboratory, NASA Goddard Space Flight Center, Greenbelt, MD, USA

^c Earth System Science Interdisciplinary Center, University of Maryland, College Park, MD, USA

^d Geospatial Sciences Center of Excellence, South Dakota State University, Brookings, SD, USA

^e Southwest Watershed Research Center, Agricultural Research Service, USDA, Tucson, AZ, USA

^f School of Public and Environmental Affairs, Indiana University, Bloomington, IN, USA

^g Institute of Arctic Biology, University of Alaska, Fairbanks, AK, USA

^h Battelle Memorial/NEON Project, Boulder, CO, USA

ARTICLE INFO

Keywords:

MODIS
VIIRS
Long-term continuity
BRDF
Albedo
NBAR

ABSTRACT

Bidirectional Reflectance Distribution Function (BRDF) model parameters, Albedo quantities, and Nadir BRDF Adjusted Reflectance (NBAR) products derived from the Visible Infrared Imaging Radiometer Suite (VIIRS), on the Suomi-NPP (National Polar-orbiting Partnership) satellite are evaluated with spatially representative *in situ* tower albedometer measurements and through comparison with the MODerate Resolution Imaging Spectroradiometer (MODIS) long term record. White Sky Albedo (WSA), Black Sky Albedo (BSA), NBAR, and Quality Assurance (QA) results show that the VIIRS algorithm is performing well at the global scale and is able to provide global data products comparable with the heritage MODIS (with an absolute bias of 0.0069 for short-wave broadband WSA) despite the spectral, angular, and effective spatial resolution differences between the two sensors. Both VIIRS and MODIS albedo are shown to agree well with *in situ* albedo measurements at a number of spatially representative sites. This evaluation provides confidence that the high quality, daily VIIRS BRDF model parameters, Albedo, and NBAR products will be able to provide the long term continuity required by the modeling and monitoring communities.

1. Introduction

Land surface albedo, defined as the ratio of upwelling to downwelling radiative flux, is an essential climate variable required to accurately model the global surface energy budget (Dickinson, 1983, 2008). To estimate albedo from remotely sensed observations, the intrinsic variability in the reflective character of the surface, which can be described by the Bidirectional Reflectance Distribution Function (BRDF), must first be considered (Nicodemus et al., 1977). To do so, a sufficient number of well distributed angular reflectances are required to adequately sample the character of the surface anisotropy and retrieve high quality surface BRDF models. Different satellites employ different acquisition strategies. Certain sensors are designed to obtain multiple angular views of a surface instantaneously, such as POLDER (Polarization and Directionality of Earth Reflectances) (Hauteœur and

Leroy, 1998) and MISR (Multi-angle Imaging SpectroRadiometer) (Diner et al., 1998). However, for cross-track scanning sensors that only obtain one or two observations of a given location each day, such as AVHRR (the Advanced Very High Resolution Radiometer) (D'Entremont et al., 1999; Sütterlin et al., 2015), MODIS (the MODerate Resolution Imaging Spectroradiometer) (Schaaf et al., 2002, 2011), and VIIRS (the Visible Infrared Imaging Radiometer Suite), a period of multiple days is needed to accumulate sufficient high quality observations (Diner et al., 1999).

MODIS instruments onboard the Terra and Aqua platforms have been providing operational BRDF model parameters, Albedo, and Nadir BRDF adjusted Reflectance (NBAR) products (MCD43) since 2000 (Schaaf et al., 2002). The operational MCD43 algorithm uses multiday, multispectral, cloud-cleared, atmospherically-corrected surface reflectances from both Terra and Aqua to fit the Ross Thick-Li Sparse-

* Corresponding author at: School for the Environment, University of Massachusetts Boston, 100 Morrissey Blvd., Boston, MA 02125-3393, USA.
E-mail address: yan.liu@umb.edu (Y. Liu).

Reciprocal (RTLSR) semi-empirical BRDF model and establish an appropriate BRDF model of the surface (Lucht et al., 2000). This is then used to generate intrinsic albedo values, such as the directional hemispherical reflectance at local solar noon (or Black Sky Albedo) and the bihemispherical reflectance under isotropic illumination (or White Sky Albedo) as well as NBAR values at local solar noon. To evaluate the performance of the product, tower measured albedo values from the Baseline Surface Radiation Network (BSRN), the SURface RADiation (SURFRAD) budget observing network (which serves as the USA contribution to BSRN), the Long Term Ecological Research Network (LTER), Ameriflux, and other observational networks are used as ground truth. Previous evaluation of the NASA standard MODIS albedo products has shown that they agree well with these *in situ* albedo values over a range of different land covers, including cropland, grassland, forest (Cescatti et al., 2012; Wang et al., 2014), and snow (Stroeve et al., 2005, 2013; Wang et al., 2012). When compared to ground measurements at spatially representative sites, the MODIS product is shown to meet the accuracy requirements of the climate modeling community (Dickinson, 1983; Román et al., 2013; Wang et al., 2014).

The NASA standard MODIS BRDF product (MCD43A1) has also been used to provide the BRDF parameters needed for other sensors that do not acquire enough angular information to directly calculate albedo or adequately correct view-angle effects (Roy et al., 2016). For example, Shuai et al. (2011) and Wang et al. (2016) coupled concurrent Landsat 30 m reflectances and MODIS 500 m BRDF data to generate 30 m Landsat albedos. Similarly, the Medium Resolution Imaging Spectrometer (MERIS) GlobAlbedo product utilized *a priori* anisotropy data from the MODIS BRDF product to augment the MERIS reflectances needed to produce albedos (Muller et al., 2007). A similar strategy was undertaken to produce Advanced Along-Track Scanning Radiometer (AATSR) aerosol values (Sayer et al., 2012). In addition, the MODIS albedo (MCD43A3) product has been used to improve the representation of surface albedo variability in the surface energy budget processes of global climate models (Lawrence and Chase, 2007; Morcrette et al., 2008; Myhre et al., 2005; Oleson, 2003; Yang et al., 2013), and in studies that track the ephemeral snowfall and snow melt of high latitudes (Wang et al., 2012). Likewise, the retrieval strategy used by the MCD43 product has been employed to correct for BRDF effects caused by varying illumination conditions in the VIIRS Day/Night Band nighttime radiances – namely, the surface-reflected moonlight and airglow from the Earth's upper atmosphere. This allows for the VIIRS-derived nighttime lights to be retrieved year round at the native resolutions necessary to capture anthropogenic sources of light emissions (Román and Stokes, 2015). The NBAR product (MCD43A4) has also been used for monitoring phenological changes (Shuai et al., 2013; Zhang et al., 2003, 2006), for estimating biomass (Baccini et al., 2008), and for analyzing surface vegetation structure patterns (Hill et al., 2008, 2017). Since view angle effects have been corrected out of the NBAR product, the NBAR values are used as the primary input for the MODIS land cover and phenology products (Cai et al., 2014; Friedl et al., 2010; Ganguly et al., 2010; Gray et al., 2014; Zhang et al., 2003, 2006).

The newly released and reprocessed NASA operational MODIS Collection V006 daily BRDF, Albedo, and NBAR products provide an improved temporal daily resolution (Wang et al., 2012). The algorithm preferentially weights the multiday reflectance inputs to emphasize retrievals from the center of the collection period as the day of interest. Thus, the MODIS Collection V006 daily product provides considerably more high quality full inversions than the previous 8-day MODIS Collection V005 products (Wang et al., 2012) – leading in turn to an improved temporal monitoring of vegetation phenology and snow melt (Shuai et al., 2013; Wang et al., 2012, 2014).

The VIIRS onboard the Suomi-NPP (National Polar-orbiting Partnership) satellite was launched on October 28, 2011, with the aim of building on the MODIS legacy and providing a continuous data record into the future (Román et al., 2011). Several different approaches

to retrieve land surface albedo have been utilized since the launch of the Suomi-NPP satellite. A Bright Pixel Surface Albedo (BPSA) algorithm, based on a direct estimation method (Liang, 2005) and requiring considerable post processing and smoothing, has been implemented by National Oceanic and Atmospheric Administration (NOAA) Interface Data Processing Segment (IDPS) (Justice et al., 2013; Wang et al., 2013). The approach presented here has been adopted by NASA and utilizes a daily algorithm similar to the MODIS Collection V006 daily algorithm to generate the VIIRS BRDF, Albedo and NBAR products. A detailed description of this VIIRS algorithm and an extensive evaluation and assessment of the VIIRS BRDF, Albedo and NBAR products are all provided in the following sections.

2. Algorithm and processing strategy

The VIIRS daily product utilizes all high-quality, cloud-cleared, atmospherically-corrected surface reflectances available over a 16-day period to identify the best fit Ross-Thick/Li-Sparse-Reciprocal (RTLSR) semi-empirical BRDF model (Roujean et al., 1992).

$$R(\theta, \nu, \phi, \lambda) = f_{iso}(\lambda) + f_{vol}(\lambda)K_{vol}(\theta, \nu, \phi) + f_{geo}(\lambda)K_{geo}(\theta, \nu, \phi) \quad (1)$$

where θ , ν and ϕ are solar zenith, view zenith and relative azimuth angles; *iso*, *vol* and *geo* are the isotropic, volumetric and geometric parameters. K_{vol} is the volumetric kernel derived from the Ross-Thick volume scattering radiative model, and K_{geo} is the geometric kernel derived from the Li-Sparse geometric shadow casting model. f_{iso} , f_{vol} and f_{geo} are spectrally dependent BRDF kernel weights (also known as BRDF model parameters) for the isotropic, volumetric and geometric kernels respectively. $R(\theta, \nu, \phi, \lambda)$ is the modeled reflectance at a given geometry (θ, ν, ϕ) of band λ . The 16 day processing period was originally chosen for MODIS as the optimal period to maximize the acquisition of cloud free observations from a combination of Terra and Aqua acquisitions (Roy et al., 2006). For consistency with MODIS, a 16-day accumulation period is also used for the VIIRS BRDF, Albedo, and NBAR products.

The cloud clear input observations are weighted based on the data quality, the observation footprint, and the proximity of the input data to the production date of interest. Observations with high solar zenith angles are excluded ($> 80^\circ$) or labeled as poor quality ($> 70^\circ$). The snow flag of the date of interest is used to decide whether a snow-free or snow retrieval should be performed, and only the corresponding snow or snow-free surface reflectances from that 16 day period are used as inputs. The Normalized Difference Snow Index (NDSI) (Hall et al., 2002) is used to differentiate fractional snow and full snow cover for the production day of interest.

If the number of observations is sufficient, a full retrieval is attempted to retrieve the BRDF parameters f_k using the weighted reflectances (Schaf et al., 2011, 2002; Wang et al., 2012). A Least-Squares Error (LSE) function is used to establish the analytical solutions for the model parameters f_k (Lucht et al., 2000).

$$f_k(\lambda) = \sum_{i=1}^3 \left\{ \sum_{j=1}^n \frac{\rho(\theta_j, \nu_j, \phi_j, \lambda) K_i(\theta_j, \nu_j, \phi_j)}{\omega_j(\lambda)} \times \left(\sum_{i=1}^n \frac{K_i(\theta_i, \nu_i, \phi_i) K_k(\theta_i, \nu_i, \phi_i)}{\omega_i(\lambda)} \right)^{-1} \right\} \quad (2)$$

where $\rho(\theta, \nu, \phi, \lambda)$ is the observed reflectance at given geometry (θ, ν, ϕ) of band λ . $\omega_j(\lambda)$ is the weight for the *j*th observation at waveband λ .

The Root Mean Square Error (RMSE) and Weight of Determination (WoD) (Lucht and Lewis, 2000) are used to determine whether there are sufficient surface observations to adequately sample the surface anisotropy and produce a high quality full inversion BRDF model, or if instead, a poorer quality magnitude inversion retrieval should be attempted. The magnitude inversion uses *a priori* BRDF model values to produce the retrieval. The RMSE describes the deviation of the model

fits, with the larger the RMSE, the higher the uncertainty in the model fit. The WoD describes the behavior of the RTLSR models under limited and varying angular sampling conditions and depends on the angular sampling pattern of the available data. A higher WoD means lower confidence in the angular sampling pattern (Lucht and Lewis, 2000).

$$RMSE = \sqrt{\frac{\sum_{i=1}^n ((\rho(\theta_i, \nu_i, \phi_i, \lambda) - R(\theta_i, \nu_i, \phi_i, \lambda))^2 \times w_i)}{n - 3}} \quad (3)$$

$$WoD_u = [U]^T [M^{-1}][U] \quad (4)$$

where U is a vector composed of a linear model parameter, M is a matrix providing the analytical solution of inversion equations. Quality assurance thresholds of RMSE and WoD were adopted based on the quality assessments associated with the MODIS operational BRDF, Albedo, and NBAR product (Shuai et al., 2008). If a full retrieval is successful, the *a priori* BRDF (the backup) database is updated to include this retrieval.

When there are insufficient observations, or observations that do not adequately sample the surface anisotropy (as determined by the WoD), or the RMSE fits do not meet the thresholds, a lower quality magnitude inversion (the backup-algorithm) is attempted using the latest retrieved high quality full inversion as *a priori* information and minimizing the result of the following equation (Lucht et al., 2000).

$$e_m^2 = \sum_i \{\rho(\theta_i, \nu_i, \phi_i, \lambda) - qR_m(\theta_i, \nu_i, \phi_i, \lambda)\}^2 \quad (5)$$

The new observed BRDF f_k can be estimated as

$$f_k = qf_{mk} = \frac{\sum_i \rho(\theta_i, \nu_i, \phi_i, \lambda) R_m(\theta_i, \nu_i, \phi_i, \lambda)}{\sum_i R_m(\theta_i, \nu_i, \phi_i, \lambda)} f_{mk} \quad (6)$$

where f_{mk} is the most recent previously retrieved high quality full inversion BRDF parameter. $R_m(\theta_i, \nu_i, \phi_i, \lambda)$ is the simulated angular reflectance using that BRDF parameter, and q is the adjusting factor.

If there still are not enough observations to attempt a magnitude inversion (< 2 observations), the pixel is assigned and flagged as a fill value (Schaaf et al., 2011, 2002).

With BRDF parameters established for each gridded location, spectral White Sky Albedo (WSA) values, Black Sky Albedo (BSA) at local solar noon, and NBAR at local solar noon are all estimated. WSA (bi-hemispherical albedo) is defined as the intrinsic albedo in the absence of a direct illumination component but with an isotropic diffuse illumination component. The BSA (directional hemispherical albedo) is defined as the albedo at a particular solar angle in the absence of a diffuse illumination component. The blue sky albedo is the actual bi-hemispherical albedo at a particular time and atmospheric aerosol condition. With the BRDF parameters established, the surface reflectances at all view and solar angles in the geometric hemisphere can be simulated. Thus, the BSA can be calculated by integrating the reflectances of all view angles at a desired solar angle, and the WSA can be calculated by integrating reflectances at all view and solar angles. The Quality Assurance (QA) flags, including the retrieval quality, the uncertainty, and the dates used for the retrieval are also provided.

The input, the VIIRS gridded land surface reflectance product, contains nine narrow spectral bands at a 1 km spatial resolution (the moderate resolution bands: M1–M5, M7–M8 and M10–M11) and three additional narrowbands at a 500 m resolution (the imagery resolution bands: I1–I3) (Fig. 1). The 1 km scale inputs include sufficient bands to calculate a broadband product while the 500 m scale inputs do not. Thus, the BRDF and albedos can only be generated for the three broadband values (0.3–0.7 visible, 0.7–5.0 NIR, and 0.3–5.0 nm shortwave) at the 1 km scale through the use of narrowband to broadband conversion coefficients. As VIIRS has different Relative Spectral Responses (RSR) as compared to MODIS (Fig. 1), a new set of narrowband to broadband (NTB) conversion coefficients are needed.

Following the same strategy used for the MODIS product (Liang et al., 1999; Stroeve et al., 2005), the snow-free NTB conversion coefficients of VIIRS for the three broadband (Table 1) are derived using 242 snow-free spectra from the USGS digital spectral library (Clark et al., 2007), and the snow NTB conversion coefficients (Table 2) are derived using 14 snow and ice spectra from the USGS digital spectral library and 15 snow spectra measured during field work in Antarctica in 2014–2015 (Casey et al., 2012). The VIIRS RSRs are provided by the Northrop Grumman Release of October 2011 (Cao et al., 2013).

The VIIRS BRDF, Albedo and NBAR products suite includes: the BRDF parameter product – VNP43M(I)1; the quality assessment product – VNP43M(I)2; the albedo product – VNP43M(I)3; and the NBAR product – VNP43M(I)4. In addition to the VIIRS I and M bands, a gridded 1 km VIIRS broadband Day-Night Band (DNB) surface reflectance is also produced (Relative Spectral Responses (RSRs) are displayed in Fig. 1), and a DNB BRDF, Albedo and NBAR product suite (VNP43DNB*) is produced separately using similar algorithms.

3. Assessment strategy

The performance of the VIIRS products is evaluated to ensure that the algorithm is stable and produces consistently reliable results. First, the VIIRS global shortwave WSA, the true color NBAR, and the QA maps are examined. In addition, as the successor to MODIS, the VIIRS BSA, WSA, and NBAR values are compared with the MODIS products to ensure the continuity of the long term data record. The spectral, angular and spatial differences between MODIS and VIIRS are also highlighted. Finally, the VIIRS and MODIS albedos are evaluated by comparison with *in situ* albedo values from a number of spatially representative field tower sites to ensure the quantitative quality of the VIIRS products for land surface climate and biosphere modeling.

3.1. Comparison with MODIS product

As a demonstration, the BSA, WSA and NBAR quantities from MODIS and VIIRS over three Sinusoidal (SIN) tiles, h08v05, h11v04, and h16v02 (Fig. 2) are compared for similar 500 m narrow spectral bands to illustrate the similarities and differences. In addition, the WSA quantities of these same tiles are compared for the corresponding 1 km narrowbands and the three broadband. These three example tiles cover different areas of North America and Greenland, and include a variety of land covers: for tile h08v05 (southwestern USA), 58% of the land area is shrublands, 12% is grasslands, 9% is barren or sparsely vegetated, 8% is savannas, and the remaining 13% includes forest, croplands, and urban area; for tile h11v04 (upper midwestern USA), 52% of the land area is cropland, 23% is cropland and natural vegetation mosaic, 18% is forest, and the remaining 7% is grasslands and wetlands; for tile h16v01 (Greenland), 92% of the land area is covered by snow and ice, and the rest is grasslands and shrublands. The differences in the global 1 km broadband WSA quantities between the MODIS and the VIIRS values for May 9th, 2015 will be reported in a later section (Section 4.3). The RMSE and bias values demonstrate the differences between the two products. It should be noted that the sinusoidal 1 km MODIS product used in this paper is MCD43T, which is not available to the public and only used to generate the standard 30 arc sec V006 CMG product (MCD43D) through reprojection.

$$bias = \frac{\sum_{i=1}^n (VIIRS - MODIS)}{n} \quad (7)$$

3.2. Comparison with *in situ* albedo values

The performance of both the VIIRS and MODIS products over different land covers is explored by comparison with *in situ* tower

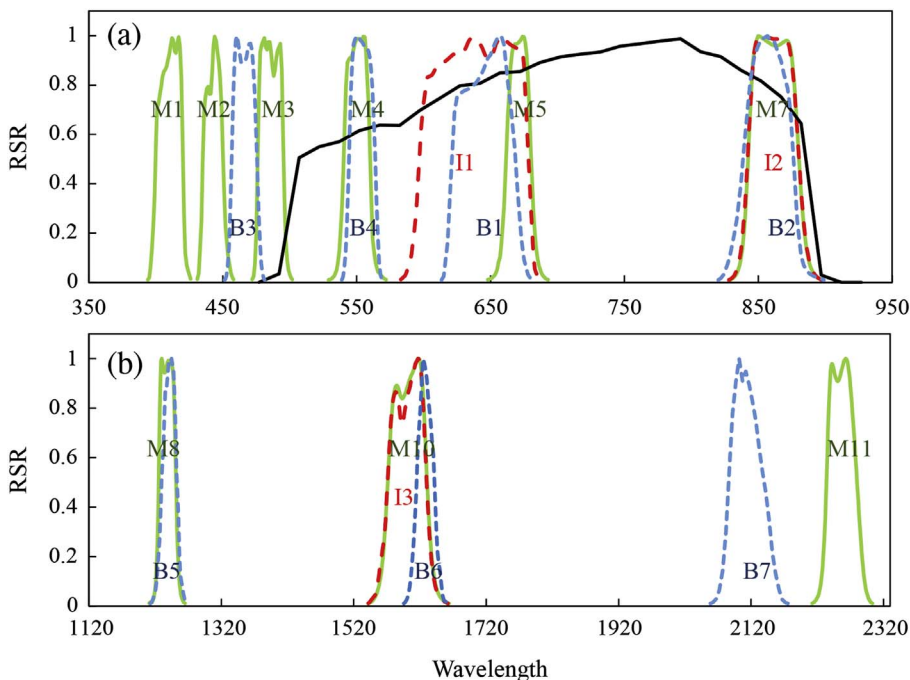


Fig. 1. Relative Spectral Responses (RSRs) of MODIS and VIIRS, the blue dashed line is the MODIS 500 m, the green line is the VIIRS 1 km, the red dashed line is the VIIRS 500 m, and the black line is the VIIRS 1 km Day-Night Band (DNB). (a) 350–950 nm, (b) 1180–2230 nm. (For interpretation of the references to color in this figure legend, the reader is referred to the web version of this article.)

Table 1
Narrowband to broadband conversion coefficients - snow free.

	M1	M2	M3	M4	M5	M7	M8	M10	M11	Intercept
Visible	0.1561	–	0.2295	0.3328	0.2815	–	–	–	–	–
NIR	–	–	–	–	–	0.5159	0.0746	0.3413	0.0890	– 0.0323
Shortwave	0.2418	– 0.2010	0.2093	0.1146	0.1348	0.2251	0.1123	0.0860	0.0803	– 0.0131

Table 2
Narrowband to broadband conversion coefficients - snow.

	M1	M2	M3	M4	M5	M7	M8	M10	M11	Intercept
Visible	0.0141	0.2380	0.1654	0.2997	0.2839	–	–	–	–	– 0.0003
NIR	–	–	–	–	–	0.5603	0.3272	– 0.3222	0.1219	0.0045
Shortwave	0.2892	– 0.4741	0.6996	–	–	0.2738	0.1463	– 0.0309	–	–

measured shortwave blue sky albedo values at sites from the Ameriflux network, the Arctic Observatory Network (AON), the Baseline Surface Radiation Network (BSRN), the National Ecological Observatory Network (NEON), and the Surface Radiation (SURFRAD) Network (Table 3).

3.2.1. In situ albedo

The *in situ* blue sky albedo at local solar noon was calculated from the measured downwelling and upwelling shortwave radiative fluxes at a range of tower sites. These values are then used to serve as evaluation data for the satellite products. The diameter of each tower radiometer

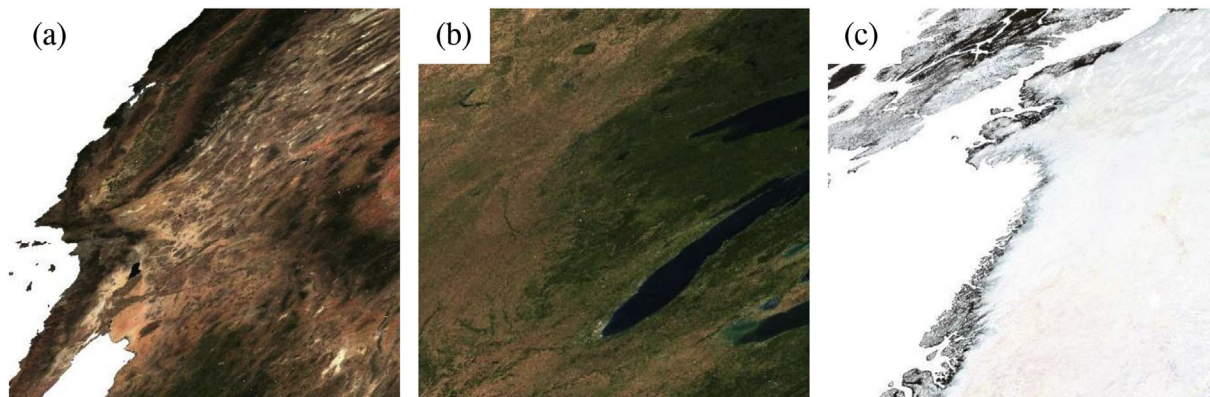


Fig. 2. True color composites of the 1 km gridded VIIRS NBAR for 2015. (a) h08v05 (southwestern USA), August 5th, R,G,B:0–0.4, (b) h11v04 (upper midwestern USA), September 26th, R,G,B:0–0.2, (c) h16v02 (Greenland), July 19th, R,G,B:0–1.0. (For interpretation of the references to color in this figure legend, the reader is referred to the web version of this article.)

Table 3
In situ sites.

Site name	Latitude	Longitude	State	Height/footprint (m)	Landcover	Network	Availability of direct and diffuse information
Santa Rita Mesquite	31.8214°N	110.8661°W	Arizona	6.5/82.08	Open shrubland	AmeriFlux	No
Morgan Monroe State Forest	39.3232°N	86.4131°W	Indiana	46/580.75	Deciduous broadleaf forest	AmeriFlux	No
Imnavait Creek Ridge	68.6068°N	149.2958°W	Alaska	2/25.25	Tundra	AON	No
Barrow	71.3226°N	156.6093°W	Alaska	4/50.50	Tundra	BSRN	Yes
Harvard Forest	42.5369°N	72.1727°W	Massachusetts	36/454.50	Mixed forests	NEON	Yes
Talladega National Forest	32.9505°N	87.3933°W	Alabama	35/441.88	Mixed forests	NEON	Yes
Desert Rock	36.6232°N	116.0196°W	Nevada	10/126.28	Desert, sparse grass	SURFRAD	Yes
Table Mountain	40.1256°N	105.2378°W	Colorado	10/126.28	Grassland	SURFRAD	Yes
Fort Peck	48.3080°N	105.1018°W	Montana	10/126.28	Grassland	SURFRAD	Yes

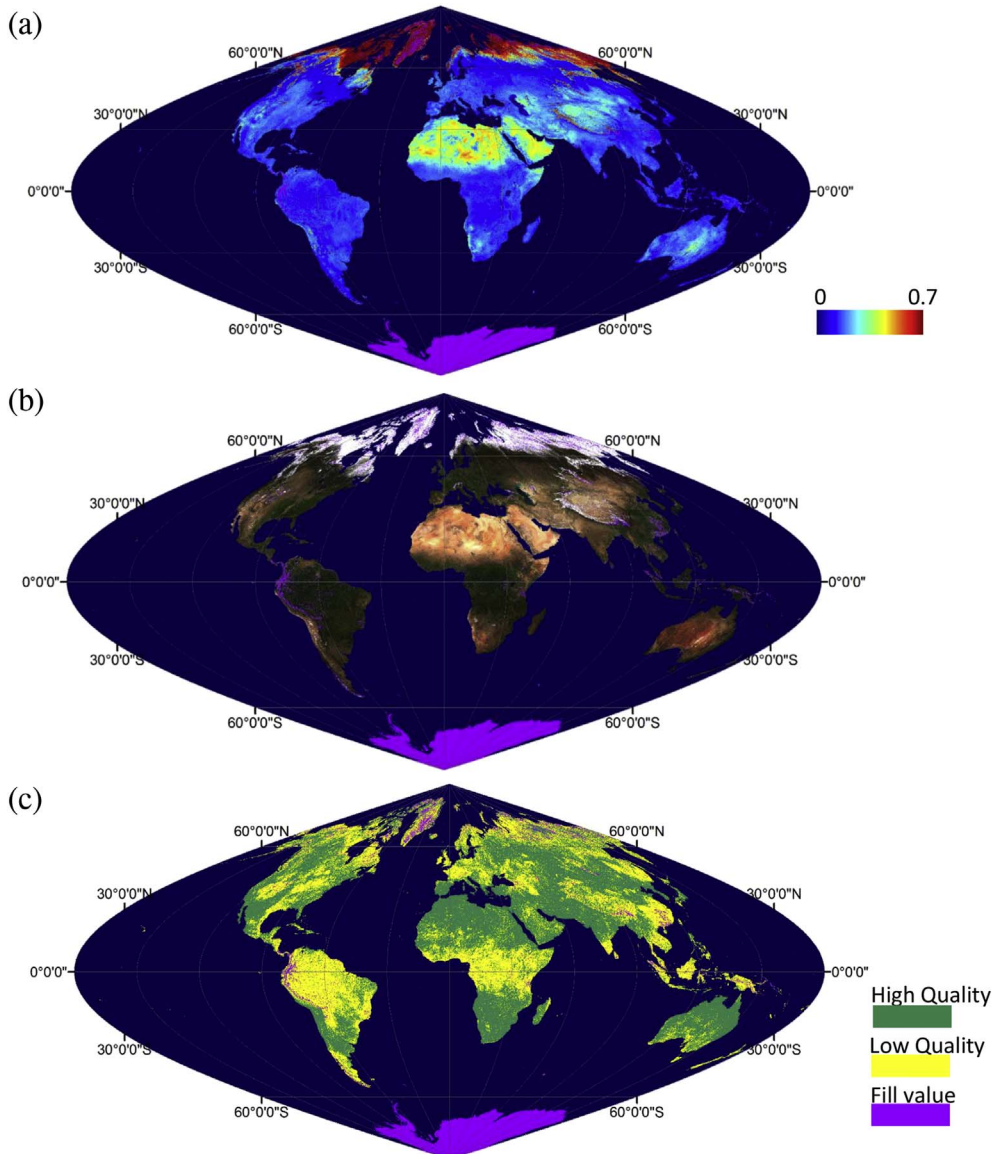


Fig. 3. Global VIIRS product for May 9th, 2015, sinusoidal projection. (a) Shortwave broadband WSA, (b) true color composite of NBAR, M5-Red, M4-Green, and M3-Blue: 0–0.4, (c) QA. The images are generated at 1 km and have been up-scaled to 10 km here for display purposes. (For interpretation of the references to color in this figure legend, the reader is referred to the web version of this article.)

footprint is controlled by the instrument height (Román et al., 2009; Shuai et al., 2011; Wang et al., 2014), as displayed in Eq. (8).

$$D = 2H \tan(FOV^\circ) \quad (8)$$

where D is the diameter of the radiometer circular footprint, H is the albedometer deployment height, and FOV is half of field of view in degree of instrument.

The footprints of the tower sites usually do not match the MODIS and VIIRS effective spatial resolution, therefore each site must be evaluated to determine whether it is spatially representative (indicating that the site is sufficiently homogeneous or homogeneously heterogeneous that it can represent the MODIS and VIIRS pixel). Wang et al. (2012, 2014) evaluated the spatial representativeness of Barrow, Fort Peck, Table Mountain, and Desert Rock using the characteristics of

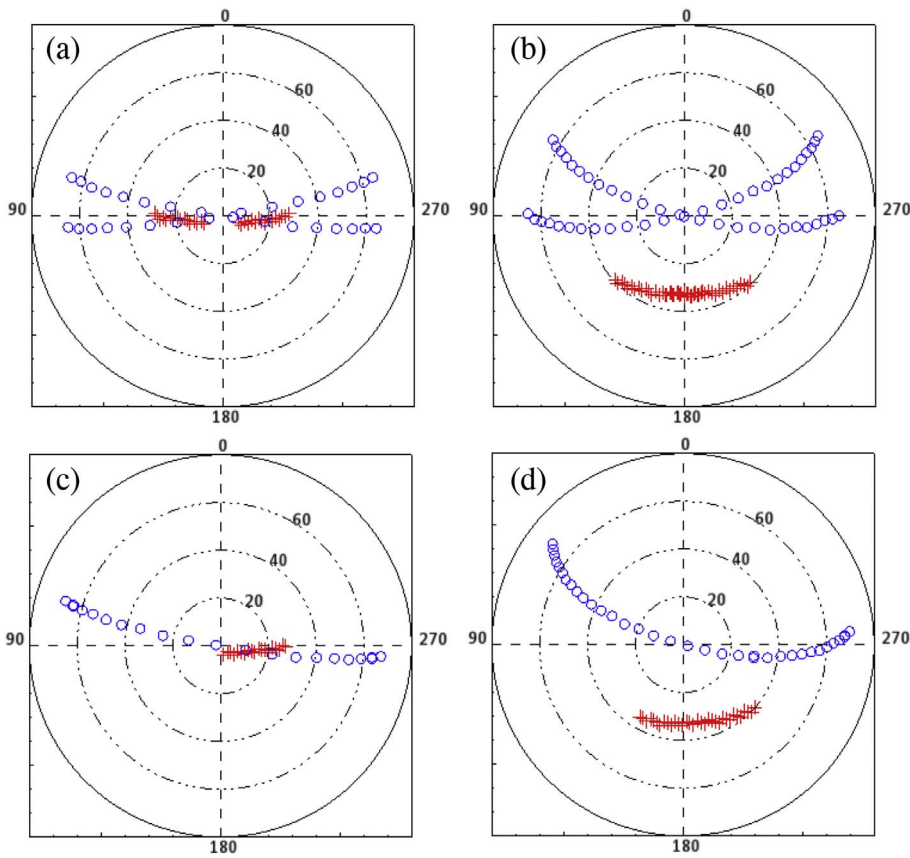


Fig. 4. Viewing geometry (blue circles) and solar geometry (red crosses) from July 4th to July 19th, 2013. (a) MODIS geometry at pixel 1, (b) MODIS geometry at pixel 2, (c) VIIRS geometry at pixel 1, (d) VIIRS geometry at pixel 2. The location of pixel 1 is at approximately latitude 0.9°N, longitude 25.0°W, close to the Equator, the location of pixel 2 is latitude 55.0°N, longitude 16.0°E, at a higher latitude. The angular coordinate is azimuth angle and the radial coordinate is zenith angle. (For interpretation of the references to color in this figure, the reader is referred to the web version of this article.)

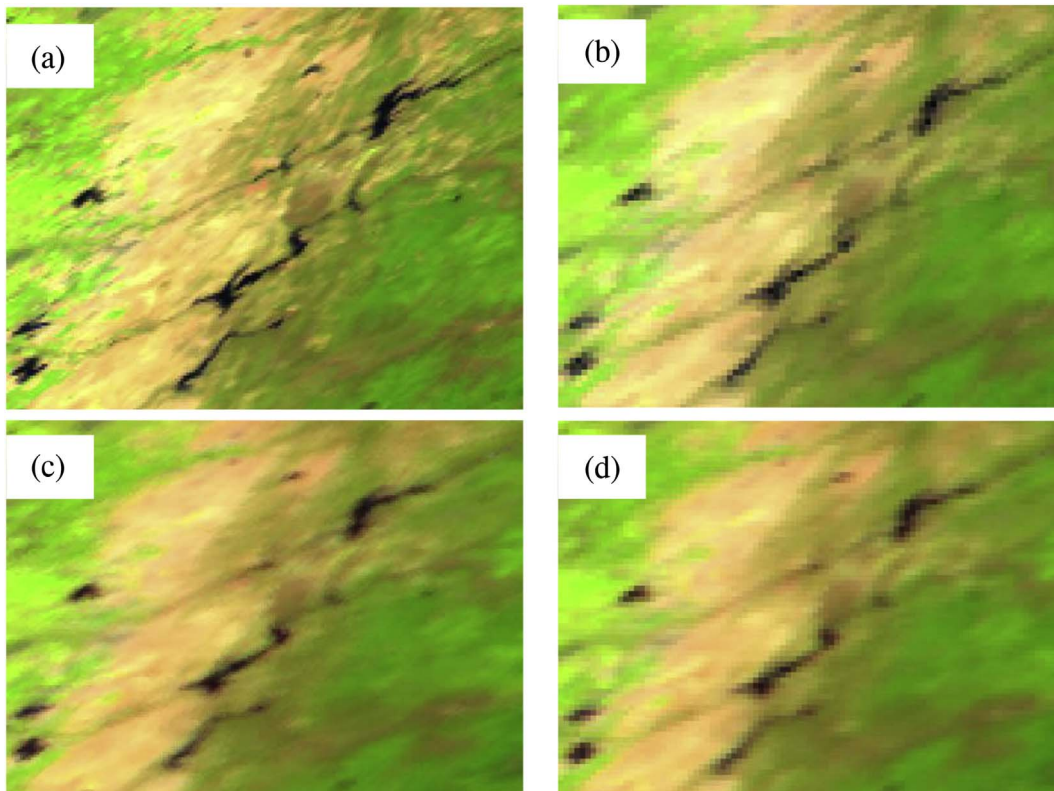


Fig. 5. The WSA for New Melones Lake and Don Pedro Reservoir in California from the (a) VIIRS 500 m, (b) VIIRS 1 km, (c) MODIS 500 m WSA, and (d) MODIS 1 km WSA. SWIR (Shortwave Infrared)-red: 0–0.42, NIR-green: 0–0.42, Red-blue: 0–0.32. (For interpretation of the references to color in this figure legend, the reader is referred to the web version of this article.)

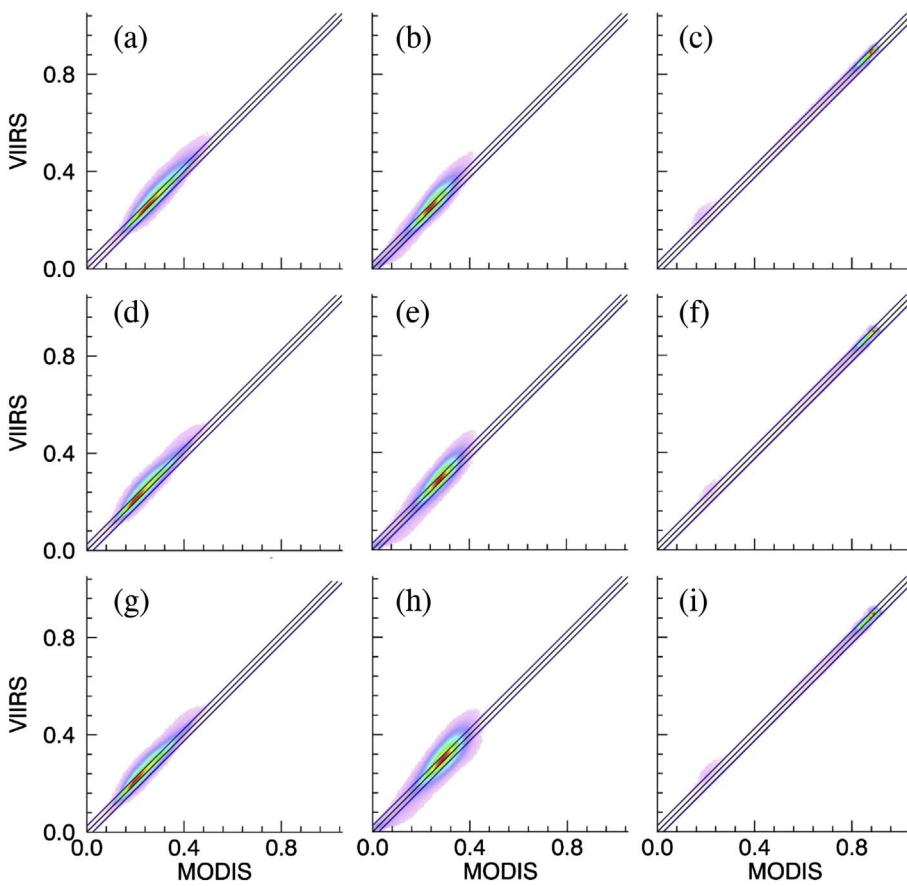


Fig. 6. The gridded 500 m narrowband density plots of MODIS band B2 vs. VIIRS band I2 for: (a) the NBAR comparison over tile 08v05, (b) h11v04, and (c) h16v01; (d) the BSA comparison over tile h08v05, (e) h11v04, and (f) h16v01; and (h) the WSA comparison over tile h08v05, (i) h11v04, and (j) h16v01. Red indicates high density and light purple indicates low density. Central lines are 1:1 lines, and outer lines are 0.025 offset lines. (For interpretation of the references to color in this figure legend, the reader is referred to the web version of this article.)

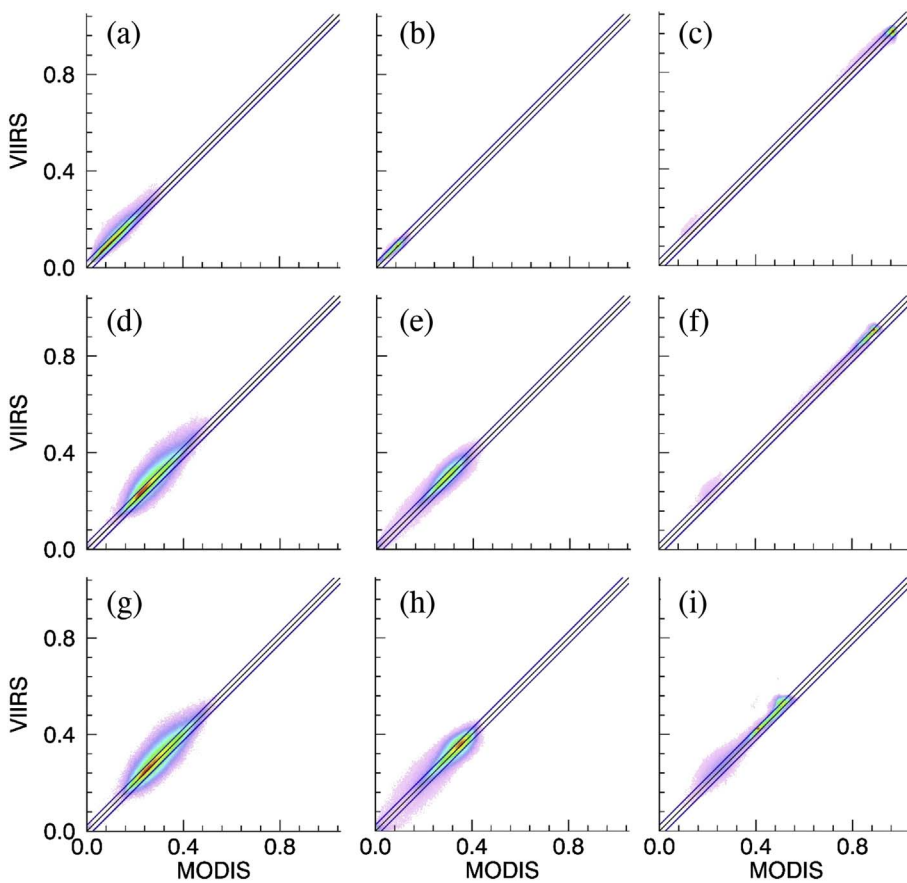


Fig. 7. (a) The gridded 1 km narrowband spectral WSA density plots of the MODIS band B4 and VIIRS band M4 over tiles h08v05, (b) h11v04, and (c) h16v02; (d) the 1 km MODIS band B2 and VIIRS band M7 over tiles h08v05, (e) h11v04, and (f) h16v02; (h) the 1 km MODIS band B5 and VIIRS band M8 over tiles h08v05, (i) h11v04, and (j) h16v02. Red indicates high density and light purple indicates low density. Central lines are 1:1 lines, and outer lines are 0.025 offset lines. The 1 km MODIS product used here is the interim product, MCD43T. (For interpretation of the references to color in this figure legend, the reader is referred to the web version of this article.)

Table 4
RMSE and bias of 500 m narrowbands (MODIS B2 vs. VIIRS I2) over selected tiles.

	RMSE			Bias		
	h08v05	h11v04	h16v01	h08v05	h11v04	h16v01
NBAR	0.0237	0.0245	0.0201	0.0130	0.0127	0.0115
BSA	0.0229	0.0255	0.0183	0.0144	0.0103	0.0073
WSA	0.0229	0.0299	0.0186	0.0144	0.0097	0.0067

Table 5
RMSE and bias of the 1 km narrowbands WSA over selected tiles.

	RMSE			Bias		
	h08v05	h11v04	h16v01	h08v05	h11v04	h16v01
MODIS B4 vs. VIIRS M4	0.0177	0.0087	0.0234	0.0069	0.0030	0.0042
MODIS B2 vs. VIIRS M7	0.0327	0.0244	0.0252	0.0152	0.0090	0.0173
MODIS B5 vs. VIIRS M8	0.0314	0.0272	0.0248	0.0072	0.0063	0.0138

The 1 km MODIS product used here is the interim product, MCD43T.

semivariograms (sill, range, and nugget effects) derived from 30 m Landsat surface reflectance at different periods of the year. Here the spatial variability of Santa Rita Mesquite, Morgan Monroe State Forest, Innvait Creek Ridge, Harvard Forest, and Talladega National Forest during the vegetation active, dormant and snow covered periods are

also evaluated using the same approach (Román et al., 2009). A variogram model (Carroll and Cressie, 1996; Davis, 2002; Matheron, 1963) is used to identify any scaling affects caused by the spatial variability of the land surface, and the analysis applies a spherical model fit to the spatial attributes derived from 30 m Landsat 8 Operational Land Imager (OLI) surface reflectances in the area surrounding the validation tower (Román et al., 2010, 2009; Wang et al., 2014; Woodcock et al., 1988a, 1988b).

3.2.2. Satellite albedo

The satellite derived BSA and WSA represent the extreme cases of completely direct and completely diffuse illumination (Lucht et al., 2000). Satellite derived blue sky albedo can be estimated by combining the WSA and BSA as a function of the fraction of diffuse sky light (Lewis and Barnsley, 1994; Lucht et al., 2000; Román et al., 2009).

$$a_{\text{blue sky}}(\lambda, \theta) = SKYL(\lambda, \theta) * a_{\text{white sky}}(\lambda) + (1 - SKYL(\lambda, \theta)) * a_{\text{black sky}}(\lambda, \theta) \tag{9}$$

where $a(\lambda, \theta)$ is the albedo at the band λ at solar zenith angle θ , WSA is not affected by solar angle, and $SKYL(\lambda, \theta)$ is the fraction of diffuse sky light at SZA θ for band λ , which can be estimated using the direct and diffuse solar radiation values recorded by the tower or the satellite measured aerosol optical depth products. The *in situ* measurements are then compared with the satellite shortwave broadband values. Among the sites mentioned in Table 3, the SURFRAD, BSRN, and NEON networks provide tower measured diffuse and direct sky light that can be directly used to calculate the fraction of diffuse sky light. However, the sites used here from Ameriflux and AON do not have that information. For those sites, the MODIS Version 006 aerosol optical depth is used to estimate the fraction of diffuse sky light.

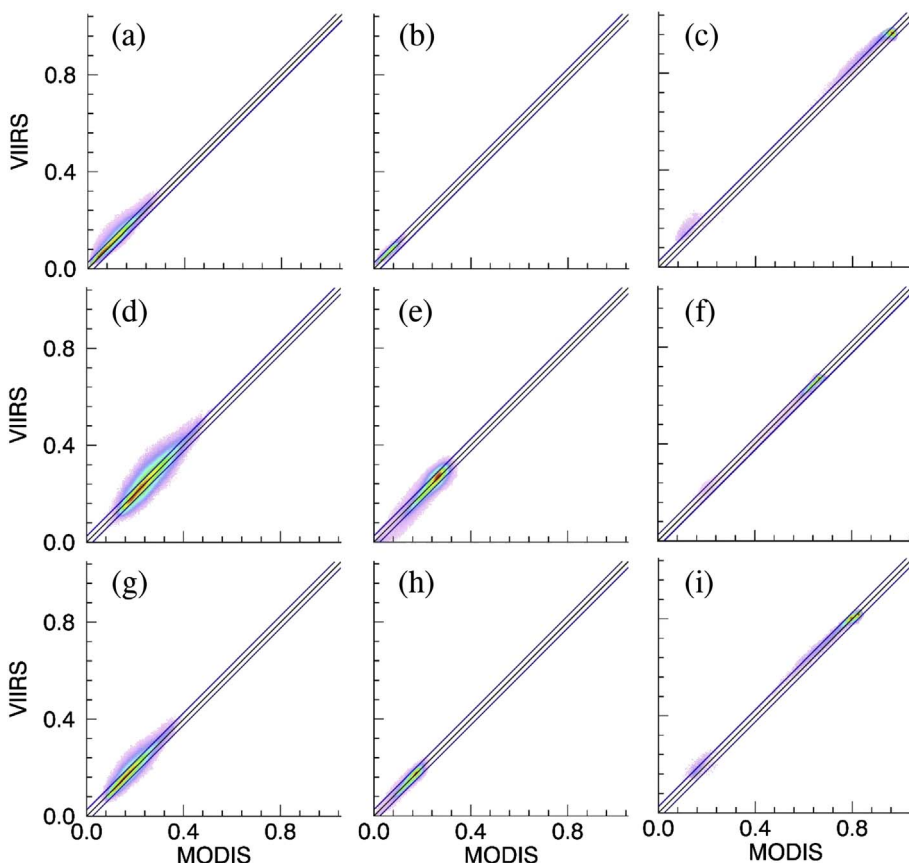


Fig. 8. (a) The gridded 1 km broadband WSA density plots for the MODIS and VIIRS visible broadband values over tiles h08v05, (b) h11v04, and (c) h16v02; (d) the MODIS and VIIRS NIR broadband values over tiles h08v05, (e) h11v04, and (f) h16v02; (h) the MODIS and VIIRS total shortwave broadband over tiles h08v05, (i) h11v04, and (j) h16v02. Red indicates high density and light purple indicates low density. Central lines are 1:1 lines, and outer lines are 0.025 offset lines. The 1 km MODIS product used here is the interim product, MCD43T. (For interpretation of the references to color in this figure legend, the reader is referred to the web version of this article.)

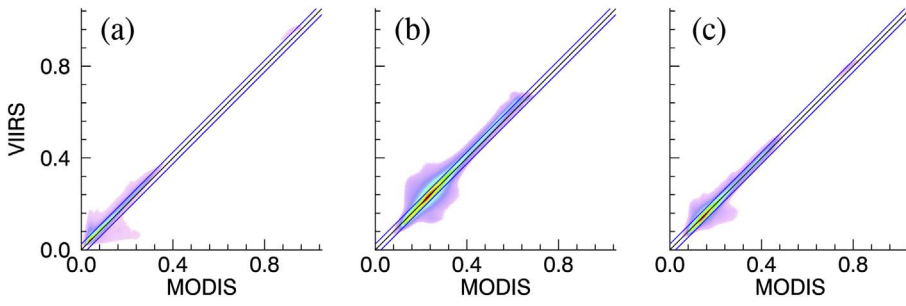


Fig. 9. (a) The gridded 1 km visible, (b) NIR, and (c) shortwave broadband WSA density plots for the MODIS and VIIRS products over the globe. Red indicates high density and light purple indicates low density. Central lines are 1:1 lines, and outer lines are 0.025 offset lines. The 1 km MODIS product used here is the interim product, MCD43T. (For interpretation of the references to color in this figure legend, the reader is referred to the web version of this article.)

Table 6
RMSE and bias of the 1 km broadband WSA over selected tiles.

	RMSE			Bias		
	h08v05	h11v04	h16v01	h08v05	h11v04	h16v01
Visible	0.0180	0.0097	0.0332	0.0103	0.0063	0.0116
NIR	0.0273	0.0200	0.0124	0.0048	0.0016	0.0029
Shortwave	0.0187	0.0116	0.0230	0.0027	−0.0010	0.0025

The 1 km MODIS product used here is the interim product, MCD43T.

Table 7
RMSE and bias of 1 km broadband WSA over the globe.

	RMSE	Bias
Visible	0.0297	0.0238
NIR	0.0357	0.0089
Shortwave	0.0274	0.0069

The 1 km MODIS product used here is the interim product, MCD43T.

Over snow, in order to consider the multiple scattering of bright surfaces, the full expression of the blue sky albedo (Eq. (10)) should be used according to the following equations: (Román et al., 2010; Wang et al., 2012)

$$A_{\lambda, \text{blue sky}}(\theta) \approx f_{\text{iso}}(\lambda) + f_{\text{vol}}(\lambda) \bar{K}_{\lambda, \text{vol}}^n(\theta) + f_{\text{geo}}(\lambda) \bar{K}_{\lambda, \text{geo}}^n(\theta) \quad (10)$$

$$\bar{K}_{\lambda, k}^n(\theta) = (1 - D_{0, \lambda}) \bar{K}_k(\theta) + D_{0, \lambda} \bar{K}_{\lambda, k}^n \quad (11)$$

$$\bar{K}_{\lambda, k}^n = \frac{1}{\pi} \int_0^{2\pi} d\phi \int_0^1 K_k(\Omega_i) N_{\text{sky}, \lambda}(\Omega_i) \mu d\mu \quad (12)$$

$$\bar{K}_k(\theta) = -\frac{1}{\pi} \int_0^{2\pi} d\phi \int_0^1 K_k(\Omega_v, \Omega_i) \mu d\mu \quad (13)$$

$A_{\lambda, \text{blue sky}}(\theta)$ is the full expression of surface albedo, $\bar{K}_{\lambda, k}^n$ is the $N_{\text{sky}, \lambda}$ weighted bihemispherical integral of $\bar{K}_k(\theta)$, and $N_{\text{sky}, \lambda}$ is the normalized sky radiance distribution under a totally absorbing lower boundary. $\bar{K}_{\lambda, k}^n(\theta)$ is the weighted sum of $\bar{K}_{\lambda, k}^n$ and $\bar{K}_k(\theta)$ for a given atmospheric condition, which is evaluated using $D_{0, \lambda}$, the proportion of diffuse illumination for a totally absorbing lower boundary. Ω_i is incident geometry, Ω_v is viewing geometry, and μ is the cosine of the incident zenith angle. And ϕ is the azimuth angle.

Only the 1 km shortwave broadband albedos from the VIIRS product and the MODIS interim product are used to compare with the *in situ* broadband albedos as VIIRS can only provide broadband values at the 1 km scale.

4. Results and discussion

4.1. Global VIIRS albedo and NBAR

The global shortwave broadband WSA, the true color NBAR, and the QA for May 9th 2015 are displayed in Fig. 3. The global VIIRS shortwave WSA Image (Fig. 3a) provides a snapshot of the differences in land-atmosphere energy exchange (for the same date) over a variety of different land covers and ecosystems worldwide. Note, the extremely high albedos over areas of ice and snow exceed the upper limit of the Fig. 3a color bar (0.7). The relatively high albedo over the Sahara Desert contrasts with the low albedos over New England mixed forests. The NBAR values (Fig. 3b) can be used to monitor the land surface patterns of vegetation phenology, photosynthetic activity, and other biophysical markers, unaffected by the effect of satellite view-angles. The QA map (Fig. 3c) shows that for this particular day, the entire continent of Antarctica is covered with fill values as a consequence of the limited daylight in late spring. Overall, excluding the continent of Antarctica, 54% of the land pixels have been retrieved with good quality (full inversion), and these are mostly distributed at mid-latitudes. The lower quality (magnitude inversion) pixels represent about 42% of the remaining land surfaces and are distributed mostly near the equator, in southern China, and at northern high latitudes. The pixels with filled values (4%) also mostly occur in the tropical areas, in southern China, and at the high latitudes. These filled pixels are generally the result of persistent cloud cover and high solar zenith angles (at high latitudes).

4.2. Differences between the MODIS and VIIRS product

Although designed for data continuity, the Suomi-NPP VIIRS instrument is not identical to the Terra and Aqua MODIS instruments. VIIRS is well calibrated (Uprety et al., 2013), and the surface reflectance uses the similar algorithm as does MODIS (Vermote et al., 2014), however the spectral, angular and spatial differences of the surface reflectance data from these two instruments can be expected to cause some differences in the retrieval of the various BRDF, Albedo and NBAR products. These differences in the input surface reflectances and in the BRDF, Albedo, NBAR products will be assessed in the following sections.

4.2.1. Differences in the input - surface reflectance

4.2.1.1. Angular differences. MODIS, onboard both the Terra and Aqua platforms, obtains data with a swath width of 2330 km in morning (with an Equator local crossing time of 10:30 a.m.) and afternoon (with an Equator local crossing time of 1:30 p.m.) orbits. In contrast, VIIRS is only onboard the single Suomi-NPP platform, with an afternoon overpass time (with an Equator local crossing time of 1:30 p.m.). While Suomi-NPP uses almost the same overpass time as does Aqua, VIIRS has a much wider swath (3040 km). Therefore, the two sensors

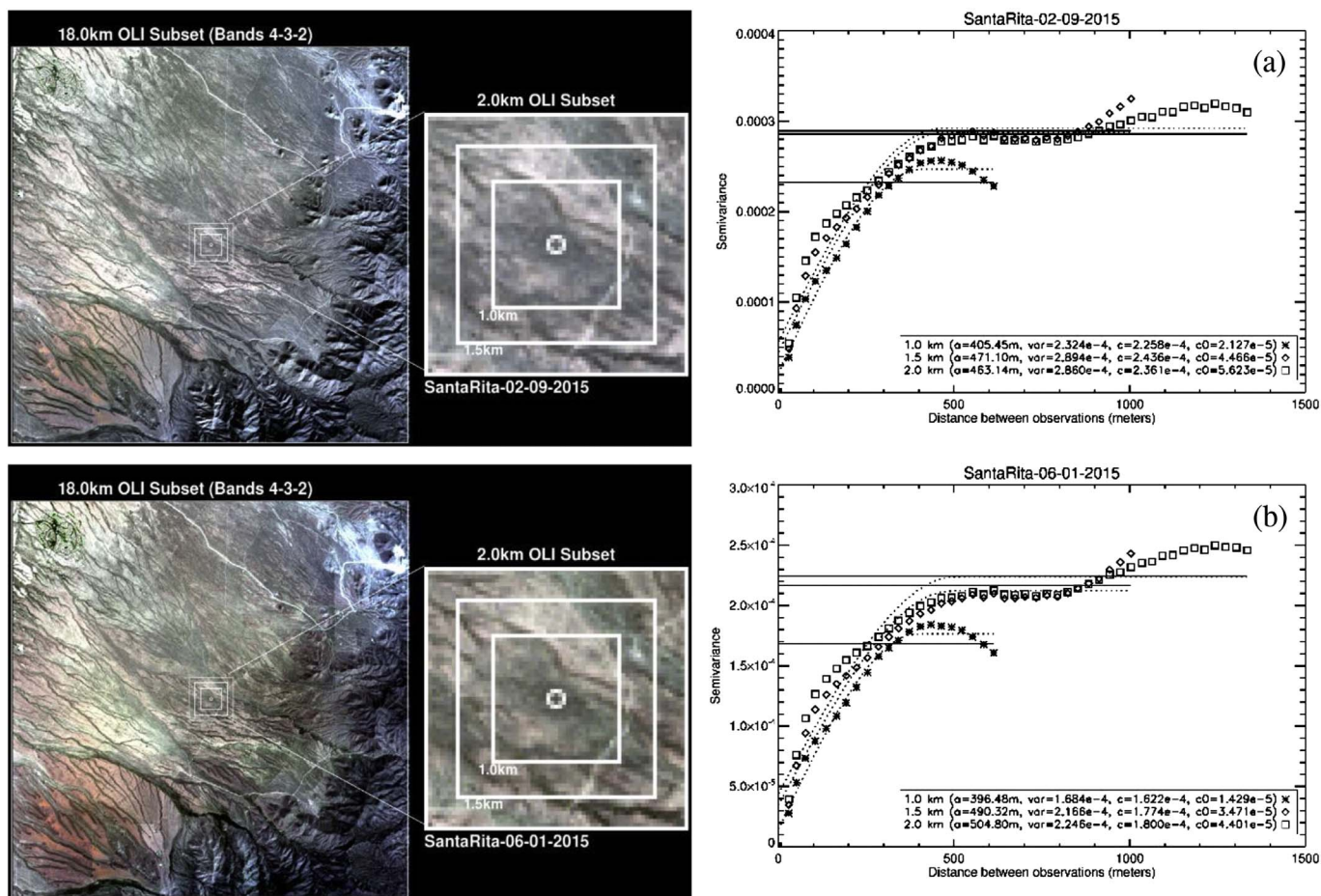


Fig. 10. Landsat 8 OLI true color composite and corresponding semivariogram functions, variogram estimator (points), spherical model (dotted curves), and sample variance (solid straight lines) using regions of 1.0 km (asterisks), 1.5 km (diamonds), and 2.0 km (squares), centered over the Santa Rita Mesquite site for (a) February 9th and (b) June 1st 2015. The circle in the left figure stands for the tower footprint.

provide different solar and viewing geometries for the same surface locations. Two pixels at different locations were selected to demonstrate the angular difference between MODIS and VIIRS surface reflectances. The first pixel (latitude 0.9°N, longitude 25.0°W) is located in the tile h17v06 close to the Equator. The second pixel (latitude 55.0°N, longitude 16.0°E) is located at a higher latitude in tile h18v03. As illustrated in Fig. 4, all of the viewing geometry (blue) and solar geometry (red) of these single pixels, as collected from July 4th to July 19th, 2013 (16 days, for the retrieval with a date of interest of July 12th) from both MODIS and VIIRS are displayed. Generally, higher latitudes have more observations than lower latitudes, however, this does not guarantee more full inversions, as cloud cover is the major factor affecting the number of valid observations. As evident from Fig. 4, two viewing geometry curves are available from MODIS (since the MODIS instrument is on two satellites) while VIIRS just has a single curve. Note again that the solar and viewing geometries of VIIRS/Suomi-NPP and MODIS/Aqua are similar, but not identical. Due to its wider swath, VIIRS can obtain more observations than a single MODIS platform (e.g. Aqua only), especially at larger viewing zenith angles, but much fewer observations than can be expected from MODIS Terra and Aqua combined.

4.2.1.2. Spatial resolution. As the BRDF, Albedo, and NBAR products are derived from multiple directional surface reflectance

measurements, the spatial resolution of the product depends on the footprint of the input surface reflectances, which vary with viewing geometry. The 500 m MODIS gridded surface reflectance values are derived from swath reflectances with footprints of approximately 500 m at nadir and these footprints grow exponentially along scan and track, reaching > 3000 m at 55° off nadir (Campagnolo and Montano, 2014). The 500 m and 1 km VIIRS gridded surface reflectances are derived from swath reflectances with nadir footprints of 375 m (the Imagery (I) bands) and 750 m (the Moderate (M) bands). However, the VIIRS onboard processing limits pixel growth in the scan direction via aggregation of sub-pixels (Wolfe et al., 2013). The MODIS Collection V006 daily 500 m BRDF, Albedo and NBAR gridded products are derived from 500 m gridded reflectance products, and the 30 arc sec geographic latitude/longitude Climate Modeling Grid (CMG) product (MCD43D) is reprojected from an interim 1 km product (MCD43T), which is not released to the public, but which makes use of all the 500 m surface reflectance observations that fall within that 1 km grid cell. Although this interim 1 km MODIS product (MCD43T) is not available for general use, we make use of the interim product in this evaluation research in order to provide realistic comparisons with the standard 1 km VIIRS products. The VIIRS 500 m and 1 km BRDF, Albedo and NBAR products are derived directly from the 500 m and 1 km VIIRS gridded surface reflectances respectively (Campagnolo et al., 2016).

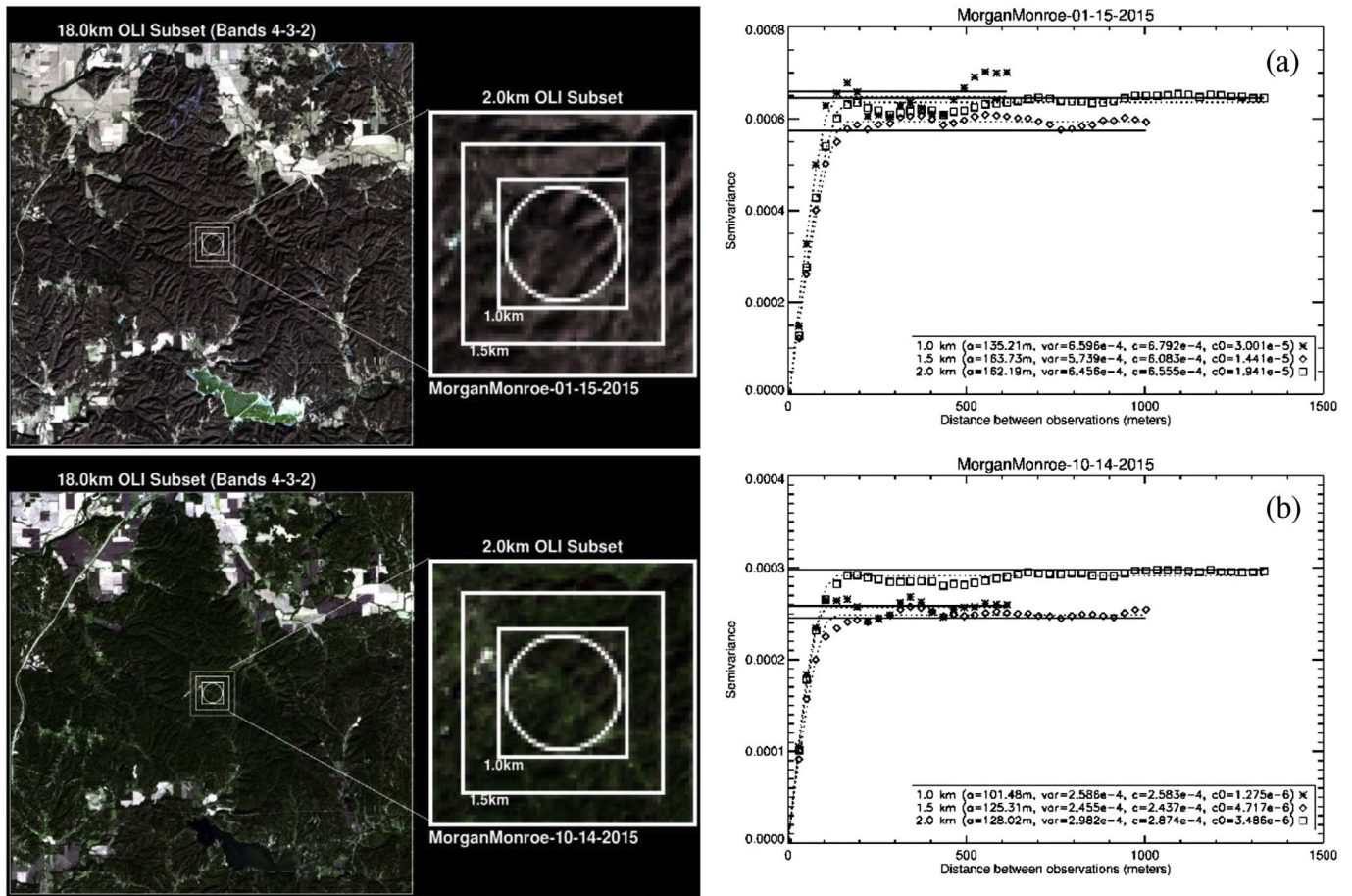


Fig. 11. Landsat 8 OLI true color composite and corresponding semivariogram functions, variogram estimator (points), spherical model (dotted curves), and sample variance (solid straight lines) using regions of 1.0 km (asterisks), 1.5 km (diamonds), and 2.0 km (squares), centered over the Morgan Monroe State Forest site for (a) January 15th and (b) October 14th 2015. The circle in the left figure stands for the tower footprint.

4.2.1.3. *Spectral differences.* MODIS and VIIRS have different band compositions (Fig. 1) and there are some offsets between bands with similar bandwidths. Four of the VIIRS band RSRs are almost identical with the MODIS band RSRs. These include: the VIIRS I2 and MODIS B2 bands (841–876 nm), the VIIRS M4 and MODIS B4 bands (545–565 nm), the VIIRS M7 and MODIS B2 band (841–876 nm), and the VIIRS M8 and MODIS B5 bands (1230–1250 nm) (Fig. 1).

4.2.2. *Differences in the output - BRDF, Albedo and NBAR products*

The differences in the angular, spatial and spectral characteristics of MODIS and VIIRS surface reflectance will result in some differences between the two products,

First, since VIIRS is only onboard one satellite, the VIIRS derived product will likely generate fewer high quality full inversions than the combined Terra and Aqua MODIS products. However, by combining VIIRS with the MODIS/Aqua observations, it may be possible to improve the retrieval of BRDF, Albedo, and NBAR after decommissioning of the older MODIS/Terra instrument (Sun, 2014). However, when additional VIIRS sensors are launched in the future as part of the JPSS program, the proportion of VIIRS full inversion will increase.

Second, as mentioned in Section 4.2.1.2, the underlying surface reflectance footprints of MODIS and of VIIRS are quite different for the same stated gridded spatial resolutions, and therefore the effective spatial resolutions for the MODIS and VIIRS BRDF, albedo and NBAR gridded products are different as well (Campagnolo et al., 2016).

In Fig. 5, the false color composite WSA of New Melones Lake and Don Pedro Reservoir in California (subset of tile h08v05), is displayed for August 8th, 2013 for MODIS and VIIRS at 500 m and 1 km. Visually, the VIIRS product is sharper compared to MODIS at the 500 m gridded scale and the 500 m VIIRS WSA has cleaner edges over lakes, rivers, and vegetation patterns than the 500 m MODIS due to the finer underlying resolution of the product. Campagnolo et al. (2016) has documented that the effective spatial resolution of the 500 m Collection V006 MODIS BRDF, Albedo, NBAR product at mid latitudes as 833 m × 618 m, while the effective resolution of the 500 m VIIRS product was determined to be 565 m × 595 m. Thus differences are to be expected over spatially heterogeneous land surface areas and along edges of contrasting land covers. Considering the 500 m gridded products, the effective resolution difference of MODIS (MCD43A) and VIIRS (VNP43I) at mid latitudes can reach 268 m × 23 m. The effective resolutions of the 1 km interim MODIS product (MCD43T) and 1 km VIIRS product (VNP43M) are 1091 m × 923 m and 1003 m × 891 m respectively. Thus the effect of spatial resolution differences for the comparison of 1 km MODIS interim albedo and VIIRS albedo is small since the effective resolution is similar.

Third, due to the spectral differences, only 4 narrowband BRDF, Albedo and NBAR products are directly comparable between the two sensors. However, separate narrowband to broadband conversion coefficients have been derived for the VIIRS channels in order to calculate appropriate broadband products from the narrowband values

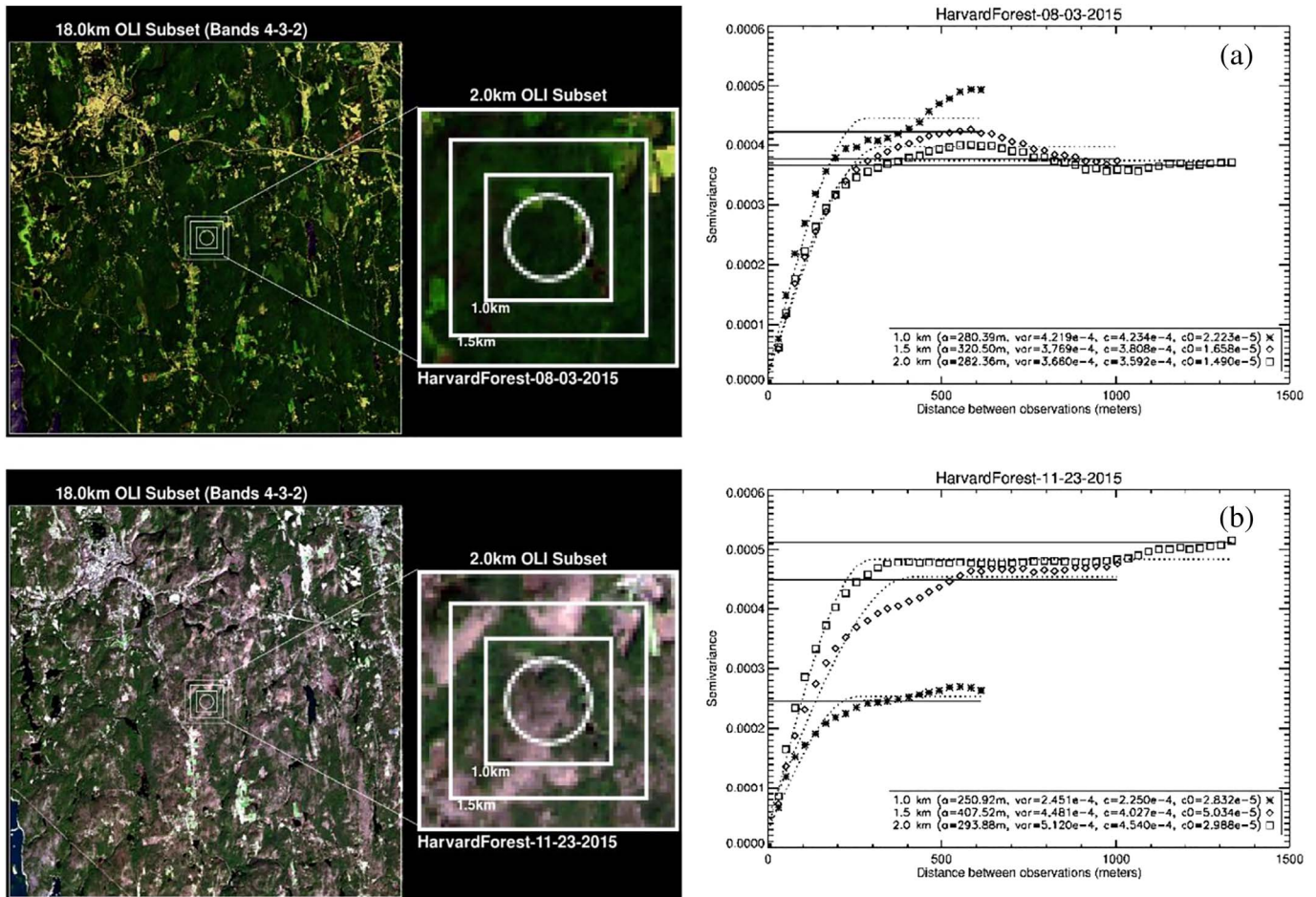


Fig. 12. Landsat 8 OLI true color composite and corresponding semivariogram functions, variogram estimator (points), spherical model (dotted curves), and sample variance (solid straight lines) using regions of 1.0 km (asterisks), 1.5 km (diamonds), and 2.0 km (squares), centered over the Harvard Forest site for (a) August 3rd and (b) November 23rd 2015. The circle in the left figure stands for the tower footprint.

(Tables 1 and 2). These can be used for comparison with the MODIS broadband values and evaluate these continuity broadband products for the modeling community in the future.

Despite these differences mentioned above, one of the major goals of these VIIRS products is to provide a continuous data record with MODIS for phenological monitoring and climate change and biospheric modeling. The following section analyzes the ability of the VIIRS products to serve as continuity products after the MODIS era.

4.3. Comparisons with the MODIS Albedo and NBAR product

The NBAR and BSA at local solar noon, and the WSA data comparisons were performed both over the aforementioned tiles (that included a number of different land covers), and over the entire globe. The density plots of the MODIS and VIIRS individual spectral NBARs, BSAs, and WSAs at gridded 500 m resolution and the WSAs at gridded 1 km resolutions for the selected tiles are displayed in Figs. 6 and 7. The associated biases and RMSE are given in Tables 4 and 5. The density plots of the MODIS interim 1 km product and the VIIRS 1 km broadband WSA values from the selected tiles and from the entire globe are displayed in Figs. 8 and 9, with the associated biases and RMSE given in Tables 6 and 7.

At the gridded 500 m scale, the narrowband density plots of NBAR, BSA, and WSA exhibit similar patterns over the selected tiles, with the

majority of the points (high quality only) falling close to the 1:1 line and within the ± 0.025 boundary (Fig. 6). The RMSE values are smaller than 0.03 (Table 4) for NBAR, BSA, and WSA. However, the VIIRS data values are consistently slightly higher than the MODIS values with small positive biases of up to 0.015 for the VIIRS I2 and MODIS B2 band comparisons over these tiles (Table 4). At the gridded 1 km scale, the majority of the WSA points also fall close to the 1:1 line and within the ± 0.025 boundary, with RMSE values ranging from 0.0087 to 0.0327 over all of the tiles and for all similar spectral bands (Table 5). Again, the VIIRS values are slightly higher than MODIS with small positive biases of up to 0.018 (Table 5). The differences in the narrow spectral band comparisons can be attributed to both the effective spatial resolution differences and the subtle RSR differences.

For the broadband values, the majority of the points (high quality only) also lie close to the 1:1 line and fall within the ± 0.025 boundary (Fig. 8) with RMSEs ranging from 0.0097 to 0.0332 (Table 6) over the selected tiles. The VIIRS broadband WSA values are also generally higher than MODIS interim broadband values with predominantly positive biases ranging from 0.0016 to 0.0116. Only the shortwave broadband values of tile h11v04 show values slightly lower than MODIS with a negative bias of -0.001 (Table 6).

At the global scale, the majority of the broadband values also lie close to the 1:1 line and fall within the ± 0.025 boundary, however, the data are quite scattered (Fig. 9). The divergence from the 1:1 line is

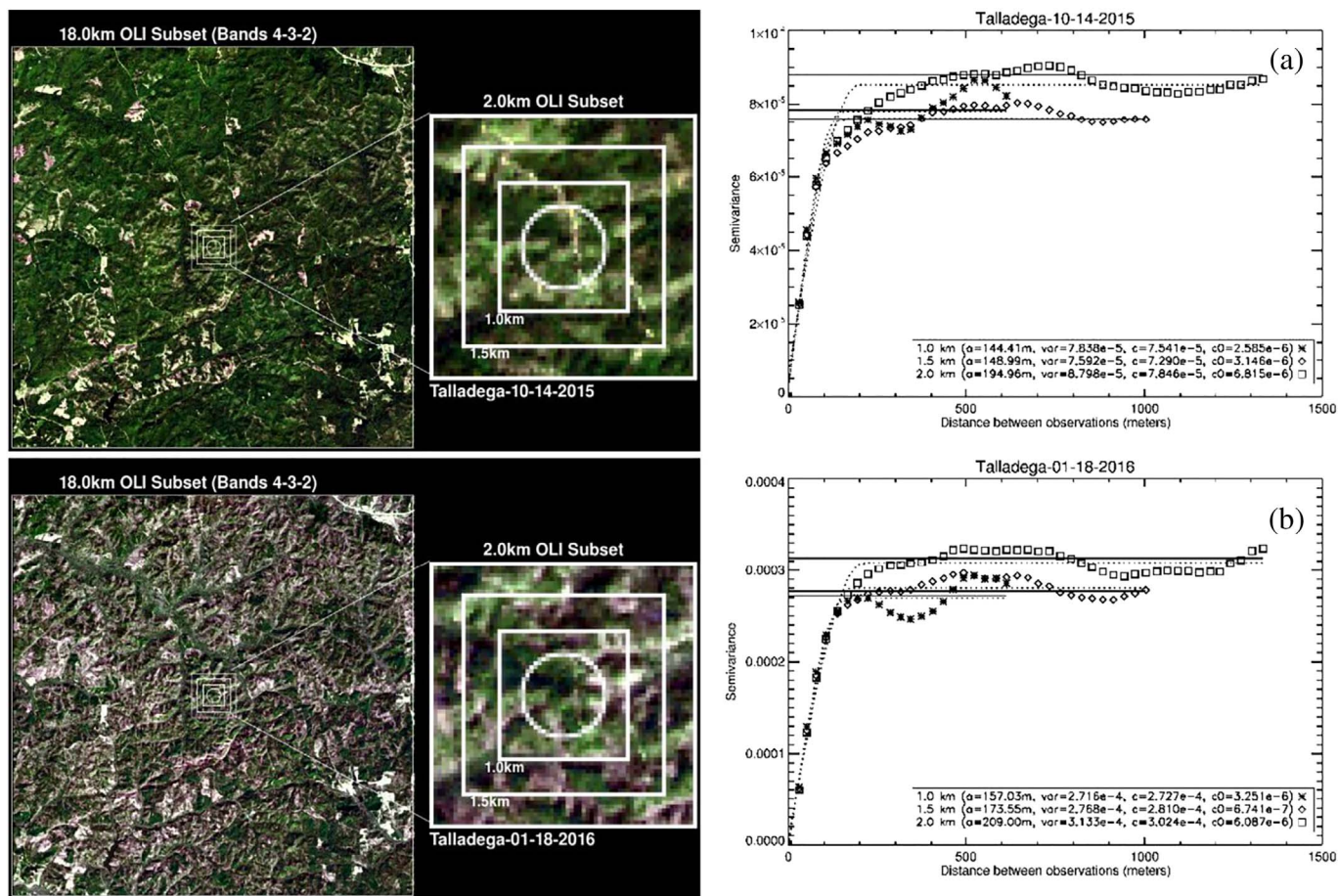


Fig. 13. Landsat 8 OLI true color composite and corresponding semivariogram functions, variogram estimator (points), spherical model (dotted curves), and sample variance (solid straight lines) using regions of 1.0 km (asterisks), 1.5 km (diamonds), and 2.0 km (squares), centered over the Talladega National Forest site for (a) October 14th, 2015 and (b) January 18th, 2016. The circle in the left figure stands for the tower footprint.

mostly related to values from the coastal zones (especially small islands), residual clouds (such as in the Amazon forest), and snow melt zones. As discussed, it is also known that the effective spatial resolution difference between the MODIS and VIIRS products adds to the scatter in these density plots. The absolute biases between the VIIRS and MODIS three broadband high quality WSA (for May 9th, 2015) are lower than 0.024 over the globe, and the absolute bias for shortwave broadband WSA is 0.0069 (Table 7). These small biases indicate that the NTB conversion coefficients being used are generally able to account for the spectral differences between MODIS and VIIRS and produce comparable broadband results.

Overall, even with the angular, spatial, and spectral differences between the two instruments, these comparisons, demonstrated over these different tiles, generate confidence that VIIRS products are capable of providing NBAR and especially broadband albedo values comparable with the MODIS products at both the gridded 500 m and 1 km scales.

4.4. Spatial representativeness of sites

The SURFRAD sites at Fort Peck, Table Mountain, and Desert Rock have already been shown to be generally spatially representative of moderate resolution satellite imagery (Wang et al., 2014). The BSRN Barrow site has also been shown to be spatially representative during the fully snow covered period, but rather heterogeneous during the

snow melt seasons (Wang et al., 2012). The spatial representativeness was reevaluated for more current dates over these sites, and the results are consistent with the earlier findings of Wang et al. (2012, 2014). The spatial representativeness of the Santa Rita Mesquite, Morgan Monroe State Forest, Innavaik Creek Ridge, Harvard Forest, and Talladega National Forest sites during the active vegetation, and the dormant and snow covered periods in the validation temporal range are all evaluated and described in this section.

The last five sites listed show good spatial representativeness at the 1 km scale. The Santa Rita Mesquite site also exhibits good spatial representativeness at the 2 km scale (Fig. 10). There is only a small deviation from the model fit in the 2 km subset, demonstrating that this site is very homogenous with variance in the mean broadband albedo values within the 2 km subset at 0.00029. The three forest sites (Morgan Monroe State Forest (Fig. 11), Harvard Forest (Fig. 12) and Talladega State Forest (Fig. 13)) all exhibit good spatial representativeness during both leaf-off and leaf-on periods. The spatial attributes fit the variogram models well and the semi-variances or sill values at the 2 km scale are well below the 0.001 threshold. The Innavaik Creek Ridge site is spatially representative during both the full snow covered and snow-free periods (Fig. 14). There is a slight deviation from the model fit at the 2 km scale during the snow free period. This is likely due to the presence of a small water body at the edge of the 2 km subset. However, even with this small deviation, the site is still spatially representative with very low semi-variance values (~ 0.0003) at all

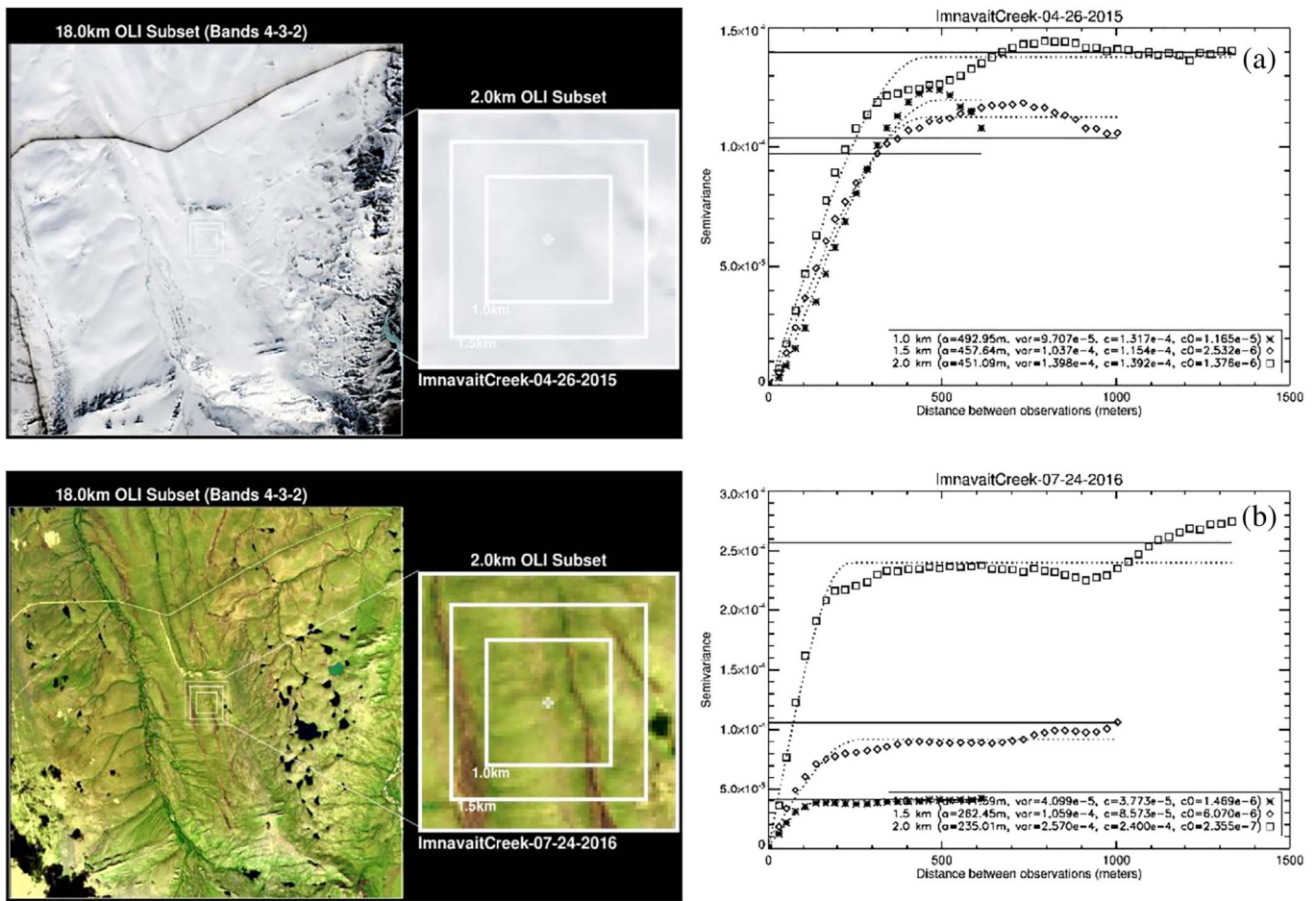


Fig. 14. Landsat 8 OLI true color composite and corresponding semivariogram functions, variogram estimator (points), spherical model (dotted curves), and sample variance (solid straight lines) using regions of 1.0 km (asterisks), 1.5 km (diamonds), and 2.0 km (squares), centered over the Innavait Creek Ridge site for (a) April 26th and (b) July 24th 2015. The circle in the left figure stands for the tower footprint.

scales. Due to their location in the southern United States, snow cover is not relevant to the Santa Rita Mesquite (Scott et al., 2009) and Talladega State Forest sites. In addition, Landsat 8 did not capture any cloud clear snow covered images over either Morgan Monroe State Forest or Harvard Forest during the validation temporal range (2015–2016), thus the spatial representativeness during the snow covered periods at these sites has not been analyzed here. Overall, all these sites are spatially representative during the snow free period with respect to both the MODIS and VIIRS satellite footprints. However, during the snow melt season and or during ephemeral snow events, the conditions can change rapidly, and these sites probably do not remain spatially representative.

4.5. Comparison with *in situ* blue sky albedo

In situ tower data from the above spatially representative sites were used to evaluate both the accuracy of the satellite derived values and assess their ability to capture the overall temporal variation in the MODIS and VIIRS albedo values.

The temporal plots of the MODIS, VIIRS, and *in situ* albedos from the Ameriflux sites of Santa Rita Mesquite, and Morgan Monroe State Forest, from the SURFRAD sites at Desert Rock, Fort Peck, and Table Mountain, from the AON site at Innavait Creek Ridge, from the NEON sites at Harvard Forest and the Talladega National Forest, and from the BSRN site at Barrow are all displayed in Fig. 15. NEON is a relatively

new network, with the Harvard Forest and Talladega National Forest towers only starting to collect data during the middle to late 2015 respectively, and thus only part of 2015 and part of 2016 are displayed for these two sites. As the Barrow site is only spatially representative during the snow covered season, only albedos during the period of DOY 60 to 180 are shown. Over all, the temporal plots of MODIS and VIIRS albedo agree well with the *in situ* measurements (Fig. 15). The Desert Rock and Santa Rita Mesquite sites are in warm semi-arid areas with bright mineral soils and rather low vegetation profiles, thus, there is less seasonal variation and few to no snow events detected by tower and satellite albedo during the year. Due to the lower cloud cover, these two sites receive more VIIRS and MODIS high quality full inversions over the year as compared to the other sites. Morgan Monroe State Forest is a deciduous forest site and thus displays more seasonal variation, with the albedo increasing with leaf out and decreasing with leaf off. Both of the MODIS and VIIRS products were able to capture this seasonal variation well and also the fractional snow event in the spring of 2015. Over the Fort Peck and Table Mountain sites, both VIIRS and MODIS agree well with the *in situ* measurements for the snow free retrievals. The majority of retrievals were poorer quality (magnitude inversions) values during the snow melt period. Even with the poorer quality results, the albedo products are able to detect these snow melt events quite well. The Innavait Creek Ridge and Barrow sites are fully covered by snow for a relatively longer period than the other sites. Therefore,

both MODIS and VIIRS provide more high quality full inversion snow albedo values at these sites during these snow covered periods. Over the Innavait Creek Ridge site, both the MODIS and VIIRS high quality full inversions agree well with the *in situ* albedos, although in this case the poorer quality magnitude inversions do not agree quite as well. Over the Barrow site, during the full snow covered season (DOY 60 to 135), both the MODIS and VIIRS retrievals provide albedos comparable to the ground observations, including those from the poor quality magnitude inversions. However, the satellite albedo and *in situ* albedo are less comparable between DOY 135 to 150 because the snow started to melt in the larger MODIS and VIIRS footprint over this site. Barrow is not spatially representative during the snow melt period (Wang et al., 2012), and the diameter of the albedometer footprint is only 50.50 m, which is considerably smaller than 1 km interim MODIS albedo and VIIRS albedo effective spatial resolutions. Also the satellite albedo values during this period are primarily poor quality results from magnitude inversions. Although both Harvard Forest and Talladega National Forest are classified as mixed forest by MODIS land cover product (MCD12Q1), the dominant vegetation of Harvard Forest is actually a deciduous temperate forest and the dominant vegetation of Talladega National Forest is actually a longleaf pine forest. Thus the Harvard Forest albedo displays more seasonal dynamics, while Talladega National Forest albedo is more stable. However, both of these conditions

are well captured by MODIS and VIIRS results. Over all, the satellite derived albedos capture most of the seasonal variations and ephemeral snow events. However, the input (surface reflectances) that result in magnitude inversions only have either limited numbers of observation or rather poor angular sampling (or both), thus the agreement of the magnitude inversions with *in situ* albedo is less ideal than the agreement with full inversions.

The comparison of the high quality (full inversion) 1 km gridded shortwave broadband albedo with the *in situ* data at all of the tower sites are presented in Fig. 16. Here, the observations occurring when the solar zenith angle is higher than 70° (the generally recommended upper limit of the satellite products (Wang et al., 2012)) and the observations with fractional snow cover, have all been removed. The snow free albedos from both VIIRS and MODIS are quite similar to the *in situ* albedo measures, with the majority of the observations lying within the ± 0.05 boundary (Fig. 16a). Also, due to the agreement between VIIRS and MODIS product, the VIIRS scatter plot is right on top the MODIS scatter plot. These comparisons show a RMSE of 0.0195 for both VIIRS and MODIS, and a bias of - 0.0034 for VIIRS and - 0.0038 for MODIS (Table 8). However, snow albedo results show greater differences with RMSE values of larger than 0.048 and absolute biases larger than 0.012 for both MODIS and VIIRS (Table 8). Overall, the 1 km MODIS and VIIRS blue sky albedos agree quite well with *in situ* measurements at these spatially representative sites.

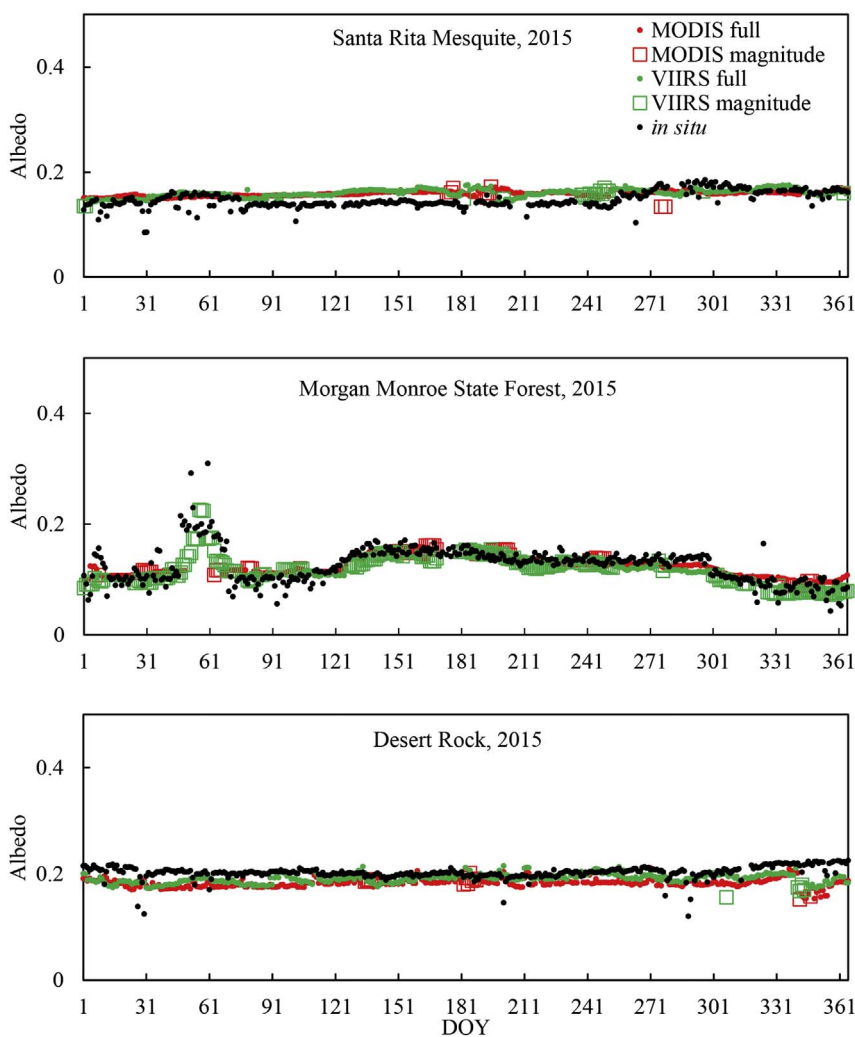


Fig. 15. Temporal comparison of the satellite derived blue sky albedo values and the *in situ* albedo values, “full” indicates the high quality, full inversions, while “magnitude” indicates the poor quality, magnitude inversions.

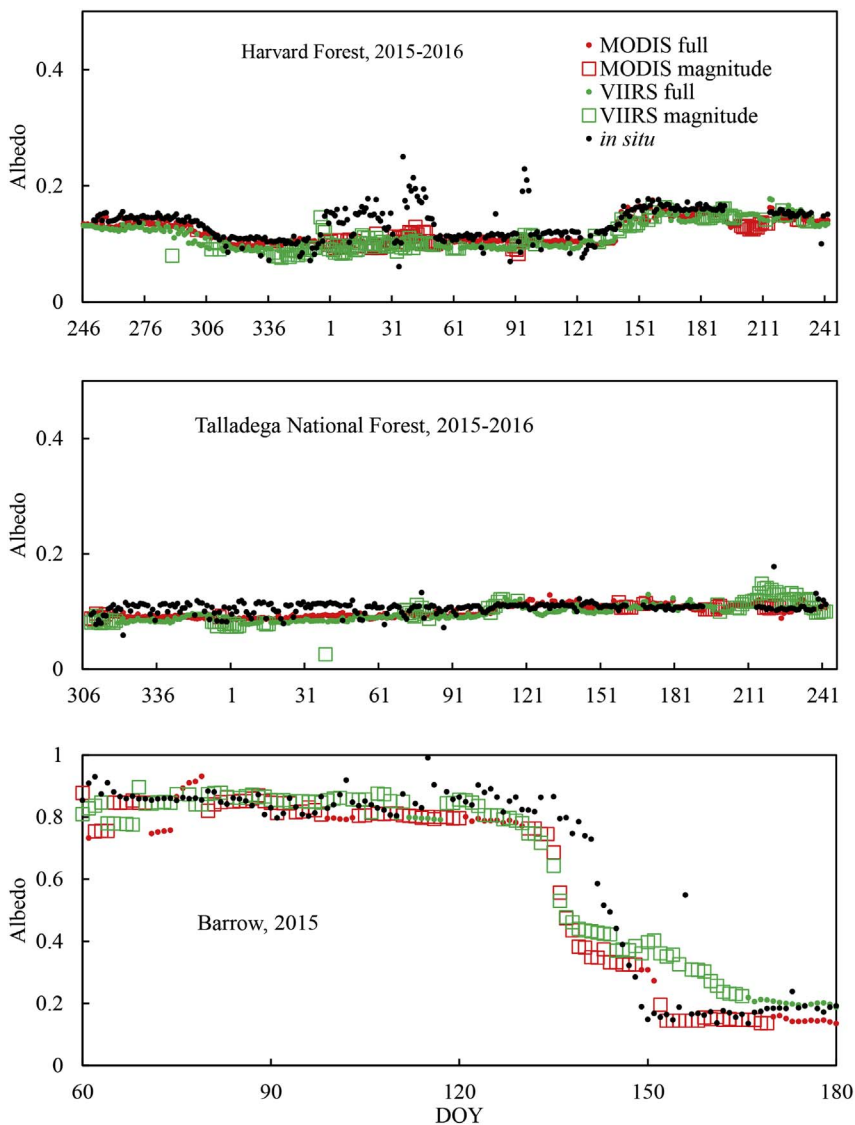


Fig. 15. (continued)

5. Conclusions

Using a retrieval strategy similar to that used with the MODIS Collection V006 products, the VIIRS daily BRDF, Albedo, and NBAR products have been delivered to the NASA Land SIPS and are now nearing production. As the MODIS sensors are aging, the community will need to rely on the VIIRS sensors in the future to provide continuous climate quality BRDF, Albedo, and NBAR records.

The VIIRS global WSA, NBAR, and QA data performs well with a majority of high quality full inversions retrieved from the VIIRS data. MODIS and VIIRS provide comparable narrowband NBAR and albedo values over various land covers and at various latitudes, with absolute biases of < 0.013 for NBAR and < 0.018 for albedo in the selected scenes. Comparisons between the MODIS interim and the VIIRS broadband albedos show that these two products are very similar with absolute biases of < 0.012 in the same selected scenes. This comparison indicates that the VIIRS daily BRDF, Albedo, and NBAR product provides the potential to extend the high quality BRDF, Albedo and NBAR product data record initiated with MODIS. Concurrent VIIRS and

MODIS blue sky albedos agree well with *in situ* tower measurements over spatially representative grassland, forest, shrub land, and tundra sites, with an RMSE of 0.0195 and an absolute bias of < 0.004 for the snow free periods. The snow albedo retrievals reflect relatively higher RMSE (> 0.048) and absolute bias (> 0.012). Overall, both MODIS and VIIRS products meet the accuracy requirements desired for albedo by climate modelers. Thus MODIS and VIIRS together can provide a long term, continuous, high quality product for the global and regional modeling communities, the vegetation and disturbance monitoring communities, and the satellite product development communities.

Additional comprehensive evaluations are planned to assure data continuity as more VIIRS observations are collected and the MODIS instruments age. These efforts will include further comparison with the MODIS daily product over larger areas and longer temporal scales, and longer term comparisons with *in situ* albedo over additional spatially representative sites. With the planned launch of the Joint Polar Satellite System (JPSS)-1 in late 2017 and JPSS-2 in late 2021 (Goldberg et al., 2013), additional VIIRS sensors will be available to provide complementary observations to strengthen this data continuity effort.

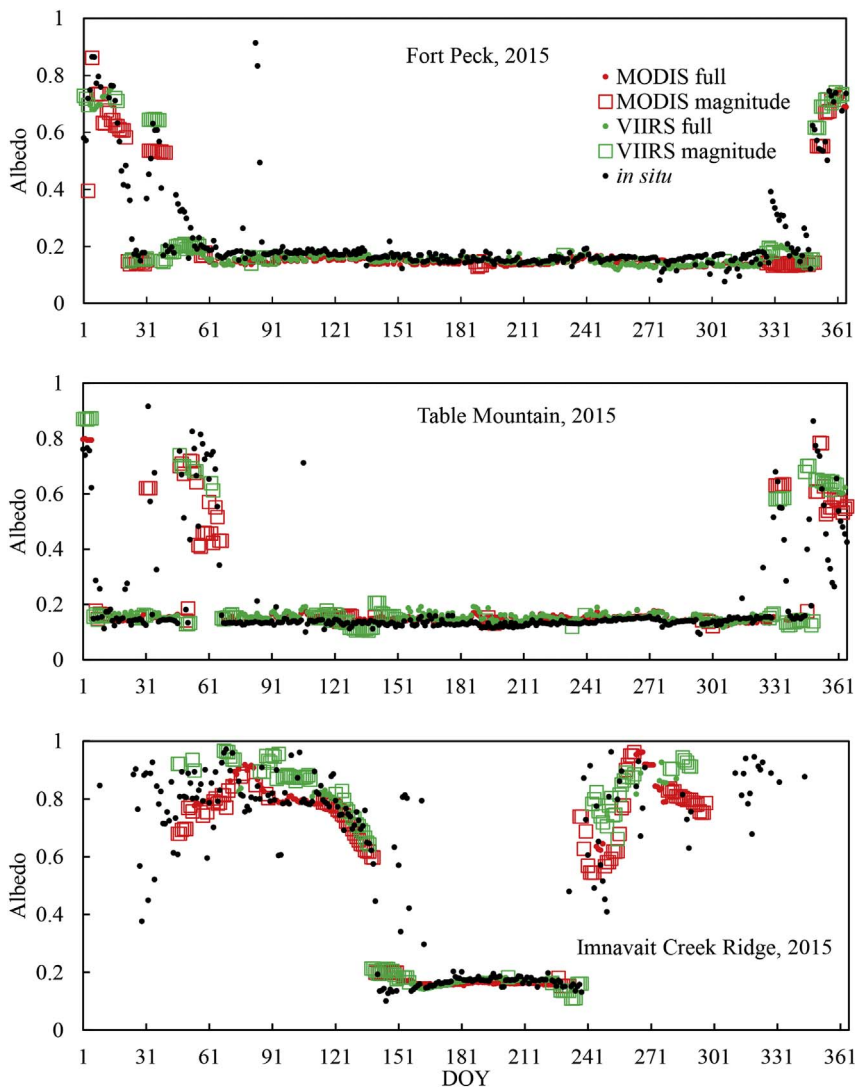


Fig. 15. (continued)

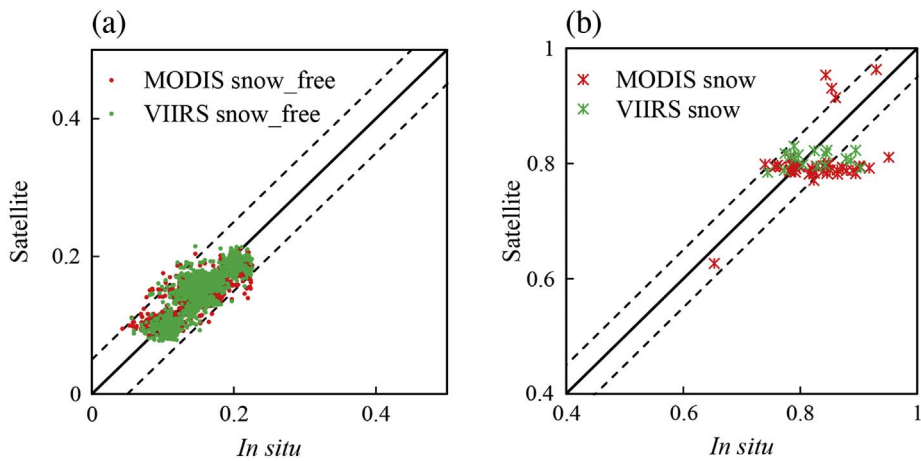


Fig. 16. Comparison of satellite and *in situ* albedo, (a) snow free, (b) snow covered. The solid line is the 1:1 line, and the dashed lines are ± 0.05 lines. The 1 km MODIS product used here is the interim product, MCD43T.

Table 8

The RMSEs of the 1 km VIIRS and MODIS blue sky albedos as compared to the *in situ* measurement.

RMSE	Snow-free			Snow		
	num-obs	RMSE	Bias	num-obs	RMSE	Bias
VIIRS	1734	0.0195	−0.0034	17	0.0488	−0.0156
MODIS	2049	0.0195	−0.0038	44	0.0626	−0.0277

The 1 km MODIS product used here is the interim product, MCD43T.

Acknowledgements

The MODIS and VIIRS processing has been supported by NASA grants NNX14AI73G and NNX14AQ18A, and the Landsat processing has been supported by USGS award G12PC00072. The authors would like to thank Colin Edgar, University of Alaska Fairbanks, for his support on providing *in situ* albedo data from Imnavait Creek Ridge.

References

- Baccini, A., Laporte, N., Goetz, S.J., Sun, M., Dong, H., 2008. A first map of tropical Africa's above-ground biomass derived from satellite imagery. *Environ. Res. Lett.* 3, 45011. <http://dx.doi.org/10.1088/1748-9326/3/4/045011>.
- Cai, S., Liu, D., Sulla-Menashe, D., Friedl, M.A., 2014. Enhancing MODIS land cover product with a spatial-temporal modeling algorithm. *Remote Sens. Environ.* 147, 243–255. <http://dx.doi.org/10.1016/j.rse.2014.03.012>.
- Campagnolo, M.L., Montano, E.L., 2014. Estimation of effective resolution for daily MODIS gridded surface reflectance products. *IEEE Trans. Geosci. Remote Sens.* 52, 5622–5632. <http://dx.doi.org/10.1109/TGRS.2013.2291496>.
- Campagnolo, M.L., Sun, Q., Liu, Y., Schaaf, C., Wang, Z., Román, M.O., 2016. Estimating the effective spatial resolution of the operational BRDF, albedo, and nadir reflectance products from MODIS and VIIRS. *Remote Sens. Environ.* 175, 52–64. <http://dx.doi.org/10.1016/j.rse.2015.12.033>.
- Cao, C., Xiong, J., Blonski, S., Liu, Q., Uprety, S., Shao, X., Bai, Y., Weng, F., 2013. Suomi NPP VIIRS sensor data record verification, validation, and long-term performance monitoring. *J. Geophys. Res. Atmos.* 118, 11664–11678. <http://dx.doi.org/10.1002/2013JD020418>.
- Carroll, S.S., Cressie, N., 1996. A comparison of geostatistical methodologies used to estimate snow water equivalent. *J. Am. Water Resour. Assoc.* 32, 267–278. <http://dx.doi.org/10.1111/j.1752-1688.1996.tb03450.x>.
- Casey, K.A., Kääh, A., Benn, D.I., 2012. Geochemical characterization of supraglacial debris via *in situ* and optical remote sensing methods: a case study in Khumbu Himalaya, Nepal. *Cryosphere* 6 (1), 85–100.
- Cescatti, A., Marcolla, B., Santhana Vannan, S.K., Pan, J.Y., Román, M.O., Yang, X., Ciaia, P., Cook, R.B., Law, B.E., Matteucci, G., Migliavacca, M., Moors, E., Richardson, A.D., Seufert, G., Schaaf, C.B., 2012. Intercomparison of MODIS albedo retrievals and *in situ* measurements across the global FLUXNET network. *Remote Sens. Environ.* 121, 323–334. <http://dx.doi.org/10.1016/j.rse.2012.02.019>.
- Clark, R.N., Swayze, G.A., Wise, R., et al., 2007. USGS digital spectral library splib06a. Data.
- Davis, J., 2002. Statistics and data analysis in geology. *Technometrics*. <http://dx.doi.org/10.1080/00401706.1987.10488290>.
- D'Entremont, R.P., Schaaf, C.B., Lucht, W., Strahler, A.H., 1999. Retrieval of red spectral albedo and bidirectional reflectance using AVHRR HRPT and GOES satellite observations of the New England region. *J. Geophys. Res.* 104, 6229–6239. <http://dx.doi.org/10.1029/1998JD200104>.
- Dickinson, R.E., 1983. Land surface processes and climate surface albedos and energy-balance. *Adv. Geophys.* 25, 305–353. <http://dx.doi.org/10.1017/CBO9781107415324.004>.
- Dickinson, R.E., 2008. Applications of terrestrial remote sensing to climate modeling. In: *Advances in Land Remote Sensing*. Springer, Netherlands, Dordrecht, pp. 445–463. http://dx.doi.org/10.1007/978-1-4020-6450-0_17.
- Diner, D.J., Beckert, J.C., Reilly, T.H., Bruegge, C.J., Conel, J.E., Kahn, R.A., Martonchik, J.V., Ackerman, T.P., Davies, R., Gerstl, S.A.W., Gordon, H.R., Muller, J., Myrneni, R.B., Sellers, P.J., Pinty, B., Verstraete, M.M., 1998. Multi-angle Imaging SpectroRadiometer (MISR) instrument description and experiment overview. *IEEE Trans. Geosci. Remote Sens.* 36, 1072–1087. <http://dx.doi.org/10.1109/36.700992>.
- Diner, D.J., Asner, G.P., Davies, R., Knyazikhin, Y., Muller, J.-P., Nolin, A.W., Pinty, B., Schaaf, C.B., Stroeve, J., 1999. New directions in earth observing: scientific applications of multiangle remote sensing. *Bull. Am. Meteorol. Soc.* 80, 2209–2228. [http://dx.doi.org/10.1175/1520-0477\(1999\)080<2209:NDIEOS>2.0.CO;2](http://dx.doi.org/10.1175/1520-0477(1999)080<2209:NDIEOS>2.0.CO;2).
- Friedl, M.A., Sulla-Menashe, D., Tan, B., Schneider, A., Ramankutty, N., Sibley, A., Huang, X., 2010. MODIS collection 5 global land cover: algorithm refinements and characterization of new datasets. *Remote Sens. Environ.* 114, 168–182. <http://dx.doi.org/10.1016/j.rse.2009.08.016>.
- Ganguly, S., Friedl, M.A., Tan, B., Zhang, X., Verma, M., 2010. Land surface phenology from MODIS: characterization of the collection 5 global land cover dynamics product.

- Remote Sens. Environ.* 114, 1805–1816. <http://dx.doi.org/10.1016/j.rse.2010.04.005>.
- Goldberg, M.D., Kilcoyne, H., Cikanek, H., Mehta, A., 2013. Joint polar satellite system: the United States next generation civilian polar-orbiting environmental satellite system. *J. Geophys. Res. Atmos.* 118, 13463–13475. <http://dx.doi.org/10.1002/2013JD020389>.
- Gray, J., Friedl, M., Froking, S., Ramankutty, N., Nelson, A., Gumma, M.K., 2014. Mapping Asian cropping intensity with MODIS. *IEEE J. Sel. Top. Appl. Earth Obs. Remote Sens.* 7, 3373–3379. <http://dx.doi.org/10.1109/JSTARS.2014.2344630>.
- Hall, D.K., Riggs, G.A., Salomonson, V.V., DiGirolamo, N.E., Bayr, K.J., 2002. MODIS snow-cover products. *Remote Sens. Environ.* 83, 181–194. [http://dx.doi.org/10.1016/S0034-4257\(02\)00095-0](http://dx.doi.org/10.1016/S0034-4257(02)00095-0).
- Hauteceœur, O., Leroy, M.M., 1998. Surface bidirectional reflectance distribution function observed at global scale by POLDER/ADEOS. *Geophys. Res. Lett.* 25, 4197–4200. <http://dx.doi.org/10.1029/1998GL900111>.
- Hill, M.J., Averill, C., Jiao, Z., Schaaf, C.B., Armston, J.D., 2008. Relationship of MISR RPV parameters and MODIS BRDF shape indicators to surface vegetation patterns in an Australian tropical savanna. *Can. J. Remote. Sens.* 34, S247–S267. <http://dx.doi.org/10.5589/m08-042>.
- Hill, M.J., Zhou, Q., Sun, Q., Schaaf, C.B., Palace, M., 2017. Relationships between vegetation indices, fractional cover retrievals and the structure and composition of Brazilian Cerrado natural vegetation. *Int. J. Remote Sens.* 38, 874–905. <http://dx.doi.org/10.1080/01431161.2016.1271959>.
- Justice, C.O., Román, M.O., Csizsar, I., Vermote, E.F., Wolfe, R.E., Hook, S.J., Friedl, M., Wang, Z., Schaaf, C.B., Miura, T., Tschudi, M., Riggs, G., Hall, D.K., Lyapustin, A.I., Devadiga, S., Davidson, C., Masuoka, E.J., 2013. Land and cryosphere products from Suomi NPP VIIRS: overview and status. *J. Geophys. Res. Atmos.* 118, 9753–9765. <http://dx.doi.org/10.1002/jgrd.50771>.
- Lawrence, P.J., Chase, T.N., 2007. Representing a new MODIS consistent land surface in the Community Land Model (CLM 3.0). *J. Geophys. Res. Biogeosci.* 112. <http://dx.doi.org/10.1029/2006JG000168>.
- Lewis, P., Barnsley, M., 1994. Influence of the sky radiance distribution on various formulations of the earth surface albedo. In: *Proc. Conf. Phys. Meas. Signatures Remote Sens.*
- Liang, S., 2005. Mapping daily snow/ice shortwave broadband albedo from moderate resolution imaging spectroradiometer (MODIS): the improved direct retrieval algorithm and validation with Greenland *in situ* measurement. *J. Geophys. Res.* 110, D10109. <http://dx.doi.org/10.1029/2004JD005493>.
- Liang, S., Strahler, A.H., Walthall, C., 1999. Retrieval of land surface albedo from satellite observations: a simulation study. *J. Appl. Meteorol.* 38, 712–725. [http://dx.doi.org/10.1175/1520-0450\(1999\)038<0712:ROLSAF>2.0.CO;2](http://dx.doi.org/10.1175/1520-0450(1999)038<0712:ROLSAF>2.0.CO;2).
- Lucht, W., Lewis, P., 2000. Theoretical noise sensitivity of BRDF and albedo retrieval from the EOS-MODIS and MISR sensors with respect to angular sampling. *Int. J. Remote Sens.* 21, 81–98. <http://dx.doi.org/10.1080/014311600211000>.
- Lucht, W., Schaaf, C.B., Strahler, A.H., 2000. An algorithm for the retrieval of albedo from space using semiempirical BRDF models. *IEEE Trans. Geosci. Remote Sens.* 38, 977–998. <http://dx.doi.org/10.1109/36.841980>.
- Matheron, G., 1963. Principles of geostatistics. *Econ. Geol.* 58, 1246–1266. <http://dx.doi.org/10.2113/gsecongeo.58.8.1246>.
- Morcrette, J.-J., Barker, H.W., Cole, J.N.S., Iacono, M.J., Pincus, R., 2008. Impact of a new radiation package, McRad, in the ECMWF integrated forecasting system. *Mon. Weather Rev.* 136, 4773–4798. <http://dx.doi.org/10.1175/2008MWR2363.1>.
- Muller, J.P., Zühlke, M., Brockmann, C., Preusker, R., Fischer, J., Regner, P., 2007. ALBEDOMAP: MERIS land surface albedo retrieval using data fusion with MODIS BRDF and its validation using contemporaneous EO and *in situ* data products. In: *Int. Geosci. Remote Sens. Symp.*, pp. 2405–2407. <http://dx.doi.org/10.1109/IGARSS.2007.4423326>.
- Myhre, G., Kvalevåg, M.M., Schaaf, C.B., 2005. Radiative forcing due to anthropogenic vegetation change based on MODIS surface albedo data. *Geophys. Res. Lett.* 32, 1–4. <http://dx.doi.org/10.1029/2005GL024004>.
- Nicodemus, F.E., et al., 1977. Geometrical considerations and nomenclature for reflectance. National Bureau of Standards, US Department of Commerce, Washington, DC.
- Oleson, K.W., 2003. Assessment of global climate model land surface albedo using MODIS data. *Geophys. Res. Lett.* 30, 3–6. <http://dx.doi.org/10.1029/2002GL016749>.
- Román, M.O., Stokes, E.C., 2015. Holidays in lights: tracking cultural patterns in demand for energy services. *Earths Future* 3 (6), 182–205.
- Román, M.O., Schaaf, C.B., Woodcock, C.E., Strahler, A.H., Yang, X., Braswell, R.H., Curtis, P.S., Davis, K.J., Dragoni, D., Goulden, M.L., 2009. The MODIS (collection V005) BRDF/albedo product: assessment of spatial representativeness over forested landscapes. *Remote Sens. Environ.* 113, 2476–2498. <http://dx.doi.org/10.1016/j.rse.2009.07.009>.
- Román, M.O., Schaaf, C.B., Lewis, P., Gao, F., Anderson, G.P., Privette, J.L., Strahler, A.H., Woodcock, C.E., Barnsley, M., 2010. Assessing the coupling between surface albedo derived from MODIS and the fraction of diffuse skylight over spatially-characterized landscapes. *Remote Sens. Environ.* 114, 738–760. <http://dx.doi.org/10.1016/j.rse.2009.11.014>.
- Román, M.O., Justice, C., Csizsar, I., Key, J.R., Devadiga, S., Davidson, C., Wolfe, R., Privette, J., 2011. Pre-launch evaluation of the NPP VIIRS land and cryosphere EDRs to meet NASA's science requirements. In: *International Geoscience and Remote Sensing Symposium (IGARSS)*, pp. 154–157. <http://dx.doi.org/10.1109/IGARSS.2011.6048921>.
- Román, M.O., Gatebe, C.K., Shuai, Y., Wang, Z., Gao, F., Masek, J.G., He, T., Liang, S., Schaaf, C.B., 2013. Use of *in situ* and airborne multiangle data to assess MODIS- and landsat-based estimates of directional reflectance and albedo. *IEEE Trans. Geosci. Remote Sens.* 51, 1393–1404. <http://dx.doi.org/10.1109/TGRS.2013.2243457>.

- Roujean, J.-L., Leroy, M., Deschamps, P.-Y., 1992. A bidirectional reflectance model of the Earth's surface for the correction of remote sensing data. *J. Geophys. Res.* 97, 20455. <http://dx.doi.org/10.1029/92JD01411>.
- Roy, D.P., Lewis, P., Schaaf, C., Devadiga, S., Boschetti, L., 2006. The global impact of clouds on the production of MODIS bidirectional reflectance model-based composites for terrestrial monitoring. *IEEE Geosci. Remote Sens. Lett.* 3, 452–456. <http://dx.doi.org/10.1109/LGRS.2006.875433>.
- Roy, D.P., Zhang, H.K., Ju, J., Gomez-Dans, J.L., Lewis, P.E., Schaaf, C.B., Sun, Q., Li, J., Huang, H., Kovalsky, V., 2016. A general method to normalize Landsat reflectance data to nadir BRDF adjusted reflectance. *Remote Sens. Environ.* 176, 255–271. <http://dx.doi.org/10.1016/j.rse.2016.01.023>.
- Sayer, A.M., Thomas, G.E., Grainger, R.G., Carboni, E., Poulsen, C., Siddans, R., 2012. Use of MODIS-derived surface reflectance data in the ORAC-AATSR aerosol retrieval algorithm: impact of differences between sensor spectral response functions. *Remote Sens. Environ.* 116, 177–188. <http://dx.doi.org/10.1016/j.rse.2011.02.029>.
- Schaaf, C.B., Gao, F., Strahler, A.H., Lucht, W., Li, X., Tsang, T., Strugnell, N.C., Zhang, X., Jin, Y., Muller, J.-P., Lewis, P., Barnsley, M., Hobson, P., Disney, M., Roberts, G., Dunderdale, M., Doll, C., d'Entremont, R.P., Hu, B., Liang, S., Privette, J.L., Roy, D., 2002. First operational BRDF, albedo nadir reflectance products from MODIS. *Remote Sens. Environ.* 83, 135–148. [http://dx.doi.org/10.1016/S0034-4257\(02\)00091-3](http://dx.doi.org/10.1016/S0034-4257(02)00091-3).
- Schaaf, C.B., Liu, J., Gao, F., Strahler, A.H., 2011. Aqua and Terra MODIS Albedo and reflectance anisotropy products. In: *Land Remote Sens. Glob. Environ. Chang.* 11, pp. 549–561. <http://dx.doi.org/10.1007/978-1-4419-6749-7>.
- Scott, R.L., Jenerette, G.D., Potts, D.L., Huxman, T.E., 2009. Effects of seasonal drought on net carbon dioxide exchange from a woody-plant-encroached semiarid grassland. *J. Geophys. Res. Biogeosci.* 114, 1–13. <http://dx.doi.org/10.1029/2008JG000900>.
- Shuai, Y., Schaaf, C.B., Strahler, A.H., Liu, J., Jiao, Z., 2008. Quality assessment of BRDF/albedo retrievals in MODIS operational system. *Geophys. Res. Lett.* 35, L05407. <http://dx.doi.org/10.1029/2007GL032568>.
- Shuai, Y., Masek, J.G., Gao, F., Schaaf, C.B., 2011. An algorithm for the retrieval of 30-m snow-free albedo from Landsat surface reflectance and MODIS BRDF. *Remote Sens. Environ.* 115, 2204–2216. <http://dx.doi.org/10.1016/j.rse.2011.04.019>.
- Shuai, Y., Schaaf, C., Zhang, X., Strahler, A., Roy, D., Morissette, J., Wang, Z., Nightingale, J., Nickeson, J., Richardson, A.D., Xie, D., Wang, J., Li, X., Strabala, K., Davies, J.E., 2013. Daily MODIS 500 m reflectance anisotropy direct broadcast (DB) products for monitoring vegetation phenology dynamics. *Int. J. Remote Sens.* 34, 5997–6016. <http://dx.doi.org/10.1080/01431161.2013.803169>.
- Stroeve, J., Box, J.E., Gao, F., Liang, S., Nolin, A., Schaaf, C., 2005. Accuracy assessment of the MODIS 16-day albedo product for snow: comparisons with Greenland in situ measurements. *Remote Sens. Environ.* 94, 46–60. <http://dx.doi.org/10.1016/j.rse.2004.09.001>.
- Stroeve, J., Box, J.E., Wang, Z., Schaaf, C., Barrett, A., 2013. Re-evaluation of MODIS MCD43 greenland albedo accuracy and trends. *Remote Sens. Environ.* 138, 199–214. <http://dx.doi.org/10.1016/j.rse.2013.07.023>.
- Sun, Q., 2014. *Assessing Change in the Earth's Land Surface Albedo With Moderate Resolution Satellite Imagery*.
- Sütterlin, M., Schaaf, C.B., Stöckli, R., Sun, Q., Hüslér, F., Neuhaus, C., Wunderle, S., 2015. Albedo and reflectance anisotropy retrieval from AVHRR operated onboard NOAA and MetOp satellites: algorithm performance and accuracy assessment for Europe. *Remote Sens. Environ.* 168, 163–176. <http://dx.doi.org/10.1016/j.rse.2015.06.023>.
- Upreti, S., Cao, C., Xiong, X., Blonski, S., Wu, A., Shao, X., 2013. Radiometric inter-comparison between Suomi-NPP VIIRS and aqua MODIS reflective solar bands using simultaneous nadir overpass in the low latitudes. *J. Atmos. Ocean. Technol.* 30, 2720–2736. <http://dx.doi.org/10.1175/JTECH-D-13-00071.1>.
- Vermote, E., Justice, C., Csizsar, I., 2014. Early evaluation of the VIIRS calibration, cloud mask and surface reflectance Earth data records. *Remote Sens. Environ.* 148, 134–145. <http://dx.doi.org/10.1016/j.rse.2014.03.028>.
- Wang, Z., Schaaf, C.B., Chopping, M.J., Strahler, A.H., Wang, J., Román, M.O., Rocha, A.V., Woodcock, C.E., Shuai, Y., 2012. Evaluation of moderate-resolution imaging spectroradiometer (MODIS) snow albedo product (MCD43A) over tundra. *Remote Sens. Environ.* 117, 264–280. <http://dx.doi.org/10.1016/j.rse.2011.10.002>.
- Wang, D., Liang, S., He, T., Yu, Y., 2013. Direct estimation of land surface albedo from VIIRS data: algorithm improvement and preliminary validation. *J. Geophys. Res. Atmos.* 118, 12,577–12,586. <http://dx.doi.org/10.1002/2013JD020417>.
- Wang, Z., Schaaf, C.B., Strahler, A.H., Chopping, M.J., Román, M.O., Shuai, Y., Woodcock, C.E., Hollinger, D.Y., Fitzjarrald, D.R., 2014. Evaluation of MODIS albedo product (MCD43A) over grassland, agriculture and forest surface types during drought and snow-covered periods. *Remote Sens. Environ.* 140, 60–77. <http://dx.doi.org/10.1016/j.rse.2013.08.025>.
- Wang, Z., Erb, A.M., Schaaf, C.B., Sun, Q., Liu, Y., Yang, Y., Shuai, Y., Casey, K.A., Román, M.O., 2016. Remote sensing of environment early spring post-fire snow albedo dynamics in high latitude boreal forests using Landsat-8 OLI data. *Remote Sens. Environ.* 185, 71–83. <http://dx.doi.org/10.1016/j.rse.2016.02.059>.
- Wolfe, R.E., Lin, G., Nishihama, M., Tewari, K.P., Tilton, J.C., Isaacman, A.R., 2013. Suomi NPP VIIRS prelaunch and on-orbit geometric calibration and characterization. *J. Geophys. Res. Atmos.* 118, 11,508–11,521. <http://dx.doi.org/10.1002/jgrd.50873>.
- Woodcock, C.E., Strahler, A.H., Jupp, D.L.B., 1988a. The use of variograms in remote sensing: I. Scene models and simulated images. *Remote Sens. Environ.* 25, 323–348. [http://dx.doi.org/10.1016/0034-4257\(88\)90108-3](http://dx.doi.org/10.1016/0034-4257(88)90108-3).
- Woodcock, C.E., Strahler, A.H., Jupp, D.L.B., 1988b. The use of variograms in remote sensing: II. Real digital images. *Remote Sens. Environ.* 25, 349–379. [http://dx.doi.org/10.1016/0034-4257\(88\)90109-5](http://dx.doi.org/10.1016/0034-4257(88)90109-5).
- Yang, J., Gong, P., Fu, R., Zhang, M., Chen, J., Liang, S., Xu, B., Shi, J., Dickinson, R., 2013. The role of satellite remote sensing in climate change studies. *Nat. Clim. Chang.* 3, 875–883. <http://dx.doi.org/10.1038/nclimate1908>.
- Zhang, X., Friedl, M.A., Schaaf, C.B., Strahler, A.H., Hodges, J.C.F., Gao, F., Reed, B.C., Huete, A., 2003. Monitoring vegetation phenology using MODIS. *Remote Sens. Environ.* 84, 471–475. [http://dx.doi.org/10.1016/S0034-4257\(02\)00135-9](http://dx.doi.org/10.1016/S0034-4257(02)00135-9).
- Zhang, X., Friedl, M.A., Schaaf, C.B., 2006. Global vegetation phenology from moderate resolution imaging spectroradiometer (MODIS): evaluation of global patterns and comparison with in situ measurements. *J. Geophys. Res. Biogeosci.* 111, 1–14. <http://dx.doi.org/10.1029/2006JG000217>.